Birth and Decline of Magma Oceans in Planetesimals: 1. Experimental Study of Erosion and Deposition of Particles in an Internally Heated Convecting Fluid

Cyril Sturtz, Angela Limare, Stephen Tait, Édouard Kaminski

JGR Planets

RESEARCH ARTICLE
10.1029/2021JE007020

Birth and Decline of Magma Oceans in Planetesimals: 2. Structure and Thermal History of Early Accreted Small Planetary Bodies

Cyril Sturtz[1], Angela Limare[1], Stephen Tait[1], and Édouard Kaminski[1]

[1]Institut de Physique du Globe de Paris, CNRS, Université Paris Cité, Paris, France

This article is a companion to Sturtz et al. (2022), https://doi.org/10.1029/2021JE007000.

Key Points:

- We model the thermal and structural evolution of radiogenic heated early accreted planetesimals that experienced an internal magma ocean
- The efficiency of crystal segregation can vary according to model parameters leading to both well-mixed and layered planetary mantles as possible outcomes
- Crustal thickening by crystal flotation increases the lifetime of the magma ocean and favors crystal segregation

Correspondence to:

C. Sturtz,
cyril.sturtz@gmail.com

Citation:

Sturtz, C., Limare, A., Tait, S., & Kaminski, É. (2022). Birth and decline of magma oceans in planetesimals: 2. Structure and thermal history of early accreted small planetary bodies. *Journal of Geophysical Research: Planets*, *127*, e2021JE007020. https://doi.org/10.1029/2021JE007020

Received 4 AUG 2021
Accepted 11 NOV 2022

Abstract This is the second of two companion papers that present a theoretical and experimental study of the thermal history of planetesimals in which heating by short-lived radioactive isotopes generates an internal magma ocean and the subsequent cooling and crystallization thereof. We study the conditions required to form and preserve basal cumulates and flotation crusts, and the implications for the thermal evolution of planetary bodies. Our model predicts that planetesimals larger than 30 km can reach 1300°C and a melt fraction of 40 vol%, producing a solid-like to liquid-like rheological transition that triggers an internal magma ocean. In the magma ocean regime core-mantle differentiation occurs very quickly and the mantle convects under a relic of chondritic material whose thickness is controlled by the temperature of rheological transition. We show that the magma ocean episode is associated with time-dependent crystal segregation and no re-entrainment. Segregation of crystals is essentially constrained by their size and by their density difference with respect to the melt, the latter being fully determined by the planetesimal's initial composition. Olivine cumulates are likely to form at the core-mantle boundary. Under certain particular conditions, a flotation crust can also form, which reduces the efficiency of heat evacuation by convection, thereby enhancing the magma ocean's lifetime and the efficiency of crystal segregation. Two types of large-scale mantle structure are possible outcomes: a well-mixed upper mantle above an olivine cumulate, or a more finely layered "onion-shell" structure.

Plain Language Summary Planetary formation occurred during the first million years after formation of the Sun. In this period, cold dust and gas accreted to form planetesimals, which themselves accreted further to form planets. When planetesimals were large enough, they undergo partial melting due to heat produced by radioactive decay of now extinct elements. If the degree of melting achieved was high enough, segregation of a metallic core occurred, leaving above it a silicate mantle bearing crystals, which behaves like a convective suspension and is called a magma ocean. In this study, we illustrate how crystals can segregate from the liquid suspension to produce a basal cumulate of dense crystals and sometimes a flotation crust of light crystals. Crystal segregation can be incomplete and part of the mantle can be well mixed. The flotation crust has an insulating effect on the planetesimal and decreases the rate at which the internally produced heat is evacuated.

1. Introduction

Planetary accretion occurred in the first million years (Myr) after the formation of calcium-aluminum inclusions (CAIs) (Baker et al., 2005; Morbidelli & Raymond, 2016). During this period, undifferentiated cold pebbles accreted to form planetesimals that further partially melted and differentiated (Kruijer et al., 2014). The degree of melting in the rocky undifferentiated body is a key parameter of planetary evolution, and is intimately linked to the heating by radioactive decay. In particular ^{26}Al and, to a much smaller extent, ^{60}Fe, produced a temperature increase that may have been large enough to induce partial melting (Neumann et al., 2012), and the formation of a metallic core by planetary-scale differentiation (Höink et al., 2006; Sahijpal et al., 2007). ^{26}Al then partitioned into the silicate mantle where the temperature continued to rise. The maximum temperature reached by a planetesimal depends mainly on the accretion time and rate and on its terminal size (Hevey & Sanders, 2006; Neumann et al., 2012; Šrámek et al., 2012) and can extend well above the solidus producing high degrees of melting. Buoyancy of the melt can induce its migration relative to the matrix. The speed of melt segregation is a function of the permeability relationship, that is, grain-size, porosity function, the melt viscosity, the melt-matrix density contrast and planetesimal gravity (McKenzie, 1984) yielding a continuum of solutions with two end members identified as the porous flow and the suspension flow (Keller & Suckale, 2019).

Several scenarios for thermal evolution are usually advocated as the result of the competition between the heating due to short-lived isotopes and the redistribution of this heat source due to its preferential partitioning into the melt and to melt migration (Lichtenberg et al., 2019). In the internal magma ocean scenario, melting occurs more rapidly than melt migration and hence affects the whole of the interior. This type of evolution is preferred for planetesimals formed soon after CAIs, with small characteristic crystal size and relatively small density difference between the melt and the solid residue. Magma sill-type of evolution should occur when melt migration keeps pace with melt production, (melt is thus extracted as it is produced) and is thus more likely for intermediate formation times ($0.5–1.75 \times t_{1/2}^{Al}$), large crystal size and high density contrast between the melt and the solid mantle. This latter scenario implies a potentially significant redistribution of ^{26}Al, which partitions into silicate melts (Wilson & Goodrich, 2012). The transfer of the major heat source into shallow magma sills results in a transient, inverted temperature profile and a thermal history distinct from the magma ocean scenario (Wilson & Keil, 2017). A third scenario of undifferentiated interior was described for planetesimals with formation time larger than $2 \times t_{1/2}^{Al}$, that experience low melt fractions. Lichtenberg et al. (2019) conclude that substantial melt segregation should not occur for grain sizes less than about 1 mm. Grain size distributions measured by Simon et al. (2018) in chondritic meteorites range between 150 and 500 microns, which favors a magma ocean outcome for early accreted planetesimals.

For the purposes of this study, we adopt the internal magma ocean scenario for early formed planetesimals with a fully molten interior of a well-mixed composition convecting beneath a thin, solid, chemically primitive lid (Dodds et al., 2021; Golabek et al., 2014; Lichtenberg et al., 2016). In this scenario processes related to core formation and differentiation occurred rapidly after the onset of convection in the planetesimal (Bryson et al., 2019). An internal magma ocean involves a mixture of silicate liquid and crystals that behaves rheologically like a fluid (Elkins-Tanton, 2012; Taylor & Norman, 1992). As long as the fraction of crystals is smaller than 60%, the magma ocean convects like a viscous suspension (Solomatov, 2000) whose effective mixture viscosity is on the order of that of the liquid component. In this regime, crystals can leave the suspension (Lavorel & Le Bars, 2009; Martin & Nokes, 1989) to form a flotation crust or a basal cumulate according to their buoyancy. The segregation of crystals eventually induces a petrological evolution of the magma ocean, and can produce a differentiated mantle.

The chemical evolution of a magma ocean is usually described using petrological models coupled with simple segregation criteria based only on the buoyancy of crystals. Heavy crystals form cumulates of dunites and/or harzburgites at the core-mantle boundary (CMB) by sedimentation (Righter & Drake, 1997), whereas light crystals accumulate at the surface, like plagioclases that formed the anorthosite crust of the Moon (Warren, 1985; Wood, 1970; Wood et al., 1970). More complex scenarios can be proposed to account for the petrological diversity of rocks encountered in asteroids. For instance, Mandler and Elkins-Tanton (2013) used a two-step model to explain the formation of heavy diogenites close to the surface of asteroid 4 Vesta through the crystallization of magma chambers that formed after the solidification of an eucritic crust. However, none of these analyses actually encompass the bulk dynamics nor the complete thermo-chemical evolution of the magma ocean. The thermal histories of these first order models are bound to remain monotonic, whereas thermal records highlight non-monotonic histories as were likely experienced by the Earth (Herzberg et al., 2010; Sleep, 2000) or by the parent body of some meteorites (Barrat & Ferrière, 2021; Yamaguchi et al., 2009, 2011). Hence, more complex and refined models are required to describe the dynamics and petrological evolution of internal magma oceans.

The aim of this paper is to show how a global modeling of thermal evolution of a mantle-scale internal magma ocean, including a physical description of the behavior of crystals in the magmatic suspension, can provide a direct explanation of structures in asteroids such as Vesta. To that aim, we use the erosion/deposition laws derived theoretically and tested experimentally in a companion paper (Sturtz, Limare, Kaminski, & Tait, 2022). After describing briefly the mechanisms that lead to the formation of a mantle-scale internal magma ocean in planetesimals, we study the formation of cumulates or flotation crusts therein by crystal/melt segregation from a convecting magma. We calculate the complete thermal history for early accreted planetesimals, and thus provide a quantitative framework to assess and predict the thermal and structural evolution of the planetesimal's interior. We study the sensitivity of planetesimal structure with respect to two main parameters: the crystal size and the planetesimal radius.

Table 1
Parameters Used in the Thermal Model

Parameters	Symbols	Values	Units	Ref.
Iron content	x_{Fe}	18	wt%	Kaminski et al. (2020)
Silicate content	$x_{\mathrm{Sil}} = 1 - x_{\mathrm{Fe}}$	82	wt%	Kaminski et al. (2020)
Chondritic abundance (^{60}Fe)	F_{Fe}	$2.14.10^{24}$	kg^{-1}	Neumann et al. (2014)
Chondritic abundance (^{26}Al)	F_{Al}	$2.62.10^{23}$	kg^{-1}	Neumann et al. (2014)
Decay energy per atom (^{60}Fe)	$\mathcal{E}_{\mathrm{Fe}}$	$4.87.10^{-13}$	J	Neumann et al. (2014)
Decay energy per atom (^{26}Al)	$\mathcal{E}_{\mathrm{Al}}$	$4.42.10^{-13}$	J	Neumann et al. (2014)
Initial ratio (^{60}Fe)	$[^{60}\mathrm{Fe}/^{56}\mathrm{Fe}]_0$	10^{-8}	-	Tang and Dauphas (2012)
Initial ratio (^{26}Al)	$[^{26}\mathrm{Al}/^{27}\mathrm{Al}]_0$	5.10^{-5}	-	Tang and Dauphas (2012)
Half life (^{60}Fe)	$t_{1/2}^{\mathrm{Fe}}$	2.6	Myr	Neumann et al. (2014)
Half life (^{26}Al)	$t_{1/2}^{\mathrm{Al}}$	0.717	Myr	Neumann et al. (2014)
Iron density	ρ_{Fe}	7,800	$\mathrm{kg\ m}^{-3}$	Kaminski et al. (2020)
Silicate density	ρ_{Sil}	3,200	$\mathrm{kg\ m}^{-3}$	Kaminski et al. (2020)
Thermal conductivity (Sil)	k_{Sil}	3	$\mathrm{W\ m}^{-1}\ \mathrm{K}^{-1}$	Kaminski et al. (2020)
Thermal conductivity (Fe)	k_{Fe}	50	$\mathrm{W\ m}^{-1}\ \mathrm{K}^{-1}$	Kaminski et al. (2020)
Thermal expansion ($\mathrm{Sil}_{(s)}$)	$\alpha_{\mathrm{Sil_s}}$	3.10^{-5}	K^{-1}	Neumann et al. (2014)
Thermal expansion ($\mathrm{Sil}_{(l)}$)	$\alpha_{\mathrm{Sil_l}}$	10^{-4}	K^{-1}	Neumann et al. (2014)
Thermal expansion (Fe)	α_{Fe}	$7.7.10^{-5}$	K^{-1}	Neumann et al. (2014)
Specific heat (Sil)	$c_{p,\mathrm{Sil}}$	1,168	$\mathrm{J\ K}^{-1}\ \mathrm{kg}^{-1}$	Neumann et al. (2012)
Specific heat (Fe)	$c_{p,\mathrm{Fe}}$	622	$\mathrm{J\ K}^{-1}\ \mathrm{kg}^{-1}$	Neumann et al. (2012)
Latent heat (Sil)	L_{Sil}	500	$\mathrm{kJ\ kg}^{-1}$	Kaminski et al. (2020)
Latent heat (Fe)	L_{Fe}	250	$\mathrm{kJ\ kg}^{-1}$	Kaminski et al. (2020)
Liquidus (Sil)	T_l^{Sil}	1,700	°C	Kaminski et al. (2020)
Solidus (Sil)	T_s^{Sil}	1,270	°C	Kaminski et al. (2020)
Liquidus (Fe)	T_l^{Fe}	1,615	°C	Kaminski et al. (2020)
Solidus (Fe)	T_s^{Fe}	990	°C	Kaminski et al. (2020)
Activation energy ($\mathrm{Sil}_{(l)}$)	$E_{a,\mathrm{Sil}}$	250	$\mathrm{kJ\ mol}^{-1}$	Kaminski et al. (2020)
Activation energy ($\mathrm{Fe}_{(l)}$)	$E_{a,\mathrm{Fe}}$	13	$\mathrm{kJ\ mol}^{-1}$	Kaminski et al. (2020)
Viscosity of iron melt at T_l^{Fe}	η_{Fe}	1	Pa s	Neumann et al. (2012)
Viscosity of silicate at $T_0 = 1000$°C	η_0	10^{18}	Pa s	Neumann et al. (2012)
Melt fraction factor for silicate	σ_{Sil}	21	-	Kaminski et al. (2020)
Crystal radius	r	$10^{-4} - 5.10^{-3}$	m	Solomatov (2000)

2. From Early Accretion to Internal Magma Ocean Episode

Planetary formation models suggest that planetesimals formed through the accretion of cold chondritic pebbles during the first few Myr after CAIs. Thermal evolution is linked to the accretion history through two important key parameters: the time at which accretion begins, and the planetesimal size (Lichtenberg et al., 2019). In the following, we consider planetesimals that accrete instantaneously at $t = 0$ Myr, characterized by mineral grain less than a few mm in size, and we study their thermal evolution as a function of their radius only.

We consider an initially undifferentiated planetesimal of radius R with mass fractions x_{Fe} of iron and x_{Sil} of silicate (Table 1). The mean density of the planetesimal ρ is given by:

$$\frac{1}{\rho} = \frac{x_{\mathrm{Fe}}}{\rho_{\mathrm{Fe}}} + \frac{x_{\mathrm{Sil}}}{\rho_{\mathrm{Sil}}}, \tag{1}$$

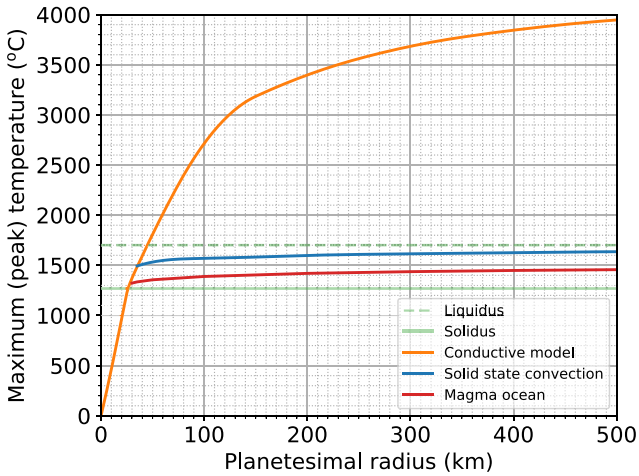

Figure 1. Peak temperature reached in early accreted planetesimals ($t_0 = 0$ Myr), heated by radiogenic elements, as a function of their radius. Three thermal models of planetesimals are shown: first, where heat is transported only by conduction (the unrealistic orange curve), second, those which experience solid-state convection (blue curve, viscosity function given by Equations 9 and 10) and those undergoing a magma ocean episode (red curve, viscosity function given by Equations 9 and 11). Magma ocean exists only for planetesimals with $R > 30$ km, as discussed in the text.

with ρ_i the density of i = Fe and Sil.

2.1. Conduction Regime

Once accreted, the planetesimal is initially at the protoplanetary disk temperature (set arbitrarily to 0°C) and undifferentiated. Its bulk thermal evolution is given by the energy budget:

$$\rho c_p \frac{\mathrm{d}T}{\mathrm{d}t} = H - \frac{3}{R} Q_s, \tag{2}$$

where c_p is the average heat capacity of the planetesimal, T is its volume-averaged temperature, H is the rate of internal heating, R is the planetesimal radius, and Q_s is the surface heat flux.

^{26}Al and ^{60}Fe are the two radiogenic isotopes active during this episode and the rate of internal heating in the undifferentiated planetesimal is given by their chondritic abundances:

$$H_{0,\mathrm{Fe}} = \rho\, F_{\mathrm{Fe}} \left[\frac{^{60}\mathrm{Fe}}{^{56}\mathrm{Fe}}\right]_0 \frac{\ln 2 \mathcal{E}_{\mathrm{Fe}}}{t^{\mathrm{Fe}}_{1/2}} e^{-t \ln 2 / t^{\mathrm{Fe}}_{1/2}}, \tag{3}$$

$$H_{0,\mathrm{Al}} = \rho\, F_{\mathrm{Al}} \left[\frac{^{26}\mathrm{Al}}{^{27}\mathrm{Al}}\right]_0 \frac{\ln 2 \mathcal{E}_{\mathrm{Al}}}{t^{\mathrm{Al}}_{1/2}} e^{-t \ln 2 / t^{\mathrm{Al}}_{1/2}}, \tag{4}$$

where F_j is the chondritic abundance of j, $[j/j]_0$ is the initial abundance of nuclides j, $\mathcal{E}_j$ is the decay energy per atom, $t^j_{1/2}$ the half life. The values used are displayed in Table 1. The surface heat flux Q_s is given by the analytical solution of the heat equation for a sphere that cools by conduction (Carslaw & Jaeger, 1959, p. 245) for a volumetric heat source with an exponential decay $H(t) = H_0 \exp(-\lambda t)$:

$$Q_s(t) = -\frac{\kappa H_0}{\lambda} \left[\sqrt{\frac{\lambda}{\kappa}} \tan^{-1/2}\left(R\sqrt{\frac{\lambda}{\kappa}}\right) - \frac{1}{R}\right] \exp(-\lambda t) - \frac{2RH_0}{\pi} \sum_{n=1}^{+\infty} \frac{\exp\left(-\frac{\kappa n^2 \pi^2 t}{R^2}\right)}{n^2 - \frac{\lambda}{\kappa}\left(\frac{R}{\pi}\right)^2}, \tag{5}$$

where κ is the average thermal diffusivity. For an undifferentiated solid body, the heat flux is given by the superposition of the heat sources given by each short-lived radioactive element.

The resulting thermal history shows that the bulk average temperature increases from zero to a maximum (peak) temperature before decreasing again to zero. The peak temperature reached in the conductive regime as a function of the planetesimal size is shown in Figure 1. One can note that conduction implies unrealistic temperatures, so high that it would imply the vapourization of planetary bodies larger than 100 km. This unrealistic conclusion can be avoided if much more efficient vertical heat transfer (by thermal convection) is taken into account.

2.2. Onset of Solid-State Convection

As temperature rises, the viscosity starts to decrease and solid-state convection can be triggered (Davies, 1980). Two characteristic dimensionless numbers describe this internally heated convective regime (Roberts, 1967): the Rayleigh-Roberts Ra_H and the Prandtl numbers Pr defined as follows:

$$Ra^*_H = \frac{\alpha \rho g H^* R^5}{\kappa \eta k}, \tag{6}$$

$$\mathrm{Pr} = \frac{\nu}{\kappa}, \tag{7}$$

with α the average thermal expansion coefficient, g the acceleration of gravity, k the average thermal conductivity, η the dynamic viscosity, $\nu = \eta/\rho$ is the kinematic viscosity, and H^* the effective rate of internal heating that takes into account secular cooling (Limare et al., 2019, 2021):

$$H^* = H - \rho c_p \frac{\mathrm{d}T}{\mathrm{d}t}. \tag{8}$$

Ra_H^* characterizes the vigor of convection and Pr quantifies the importance of inertia. The onset of convection requires two criteria. First, Ra_H^* must be larger than the critical value $Ra_{H,c}$ which, for a spherical planetesimal with rigid boundary condition, is $Ra_{H,c} = 5{,}758$ (Schubert et al., 2001). Second, in the case of strong temperature dependance of viscosity, once the critical Rayleigh-Roberts number is reached, the onset of convection is delayed but ultimately develops under a stagnant lid where heat transfer occurs by conduction (Choblet & Sotin, 2000; Davaille & Jaupart, 1993; Grasset & Parmentier, 1998; Kaminski et al., 2020).

Viscosity is the key parameter for convection in the partially molten mantle, because its variation as a function of (a) temperature, modeled by an Arrhenius law and (b) the melt content, is very large. If the degree of melting is low, typically smaller than 40%, the influence of the melt content on the viscosity can be modeled by the following law (Scott & Kohlstedt, 2006):

$$\eta(T, \phi) = \eta_0 \, f(\phi) \exp\left[\frac{E_{a,\mathrm{Sil}}}{R_g}\left(\frac{1}{T} - \frac{1}{T_0}\right)\right], \tag{9}$$

$$f(\phi) = \exp\left[-\sigma_{\mathrm{Sil}}(1 - \phi)\right], \tag{10}$$

where ϕ is the volume fraction of solid that depends on the composition and temperature, as discussed later (Equation 30), R_g is the ideal gas constant, $E_{a,\mathrm{Sil}}$ is the activation energy and σ_{Sil} is the melt fraction factor. We assume that the mantle viscosity η_0 at $T_0 = 1000°\mathrm{C}$ is 10^{18} Pa s. In the following, we assume that melt migration due to matrix compaction (McKenzie, 1984) is ineffective during radioactive heating, that is, for early accreted planetesimals, melting occurs more rapidly than melt migration (Appendix A, Figure A1b).

To account for solid-state convection, the energy budget (Equation 2) uses a surface heat flux Q_s deduced from scaling laws (see Appendix C for more details). As already discussed in Kaminski et al. (2020), we obtain that solid-state convection avoids the catastrophic thermal state predicted by the conductive regime, and maintains the temperature at "moderate," sub-liquidus values thanks to a more efficient heat transfer. The peak temperature reached in the planetesimal in the case of solid-state convection increases weakly as a function of the planetesimal radius (Figure 1). This can be explained by the fact that the ratio between the energy lost at the surface over the heat generated by radioactive decay is proportional to the surface over volume ratio, which decreases with the planetesimal radius. However, this plateau spans a temperature domain from 1500 to 1660°C, which implies a melt content of 63–92 vol% which is above that at which the solid matrix loses its interconnectivity; the description of the system by solid-state convection us no longer accurate and therefore needs to be amended.

2.3. Rheological Transition: Onset of Internal Magma Ocean Episode

Beyond a certain melt fraction, the mixture of melt and crystals behaves like a liquid or, more precisely, like a liquid suspension. The regime of convection changes beyond the rheological transition that occurs for a solid fraction of $\phi_{\mathrm{RT}} = 60\%$ for spherical crystals (Faroughi & Huber, 2015; Guazzelli & Pouliquen, 2018; Solomatov, 2000). Assuming batch melting, this critical solid content corresponds to a temperature T_{RT} that only depends on the composition of the silicate mantle of the planetesimal. For the model composition considered here and detailed in Section 4.1, $T_{\mathrm{RT}} = 1307°\mathrm{C}$.

To take into account the rheological transition, we adapt the model of Scott and Kohlstedt (2006), using a Krieger-Dougherty law (Faroughi & Huber, 2015; Guazzelli & Pouliquen, 2018; Solomatov, 2000) so that $f(\phi)$ becomes:

$$f(\phi) = \left(1 - \frac{\phi}{\phi_c}\right)^{-2.5\phi_{\mathrm{RT}}}. \tag{11}$$

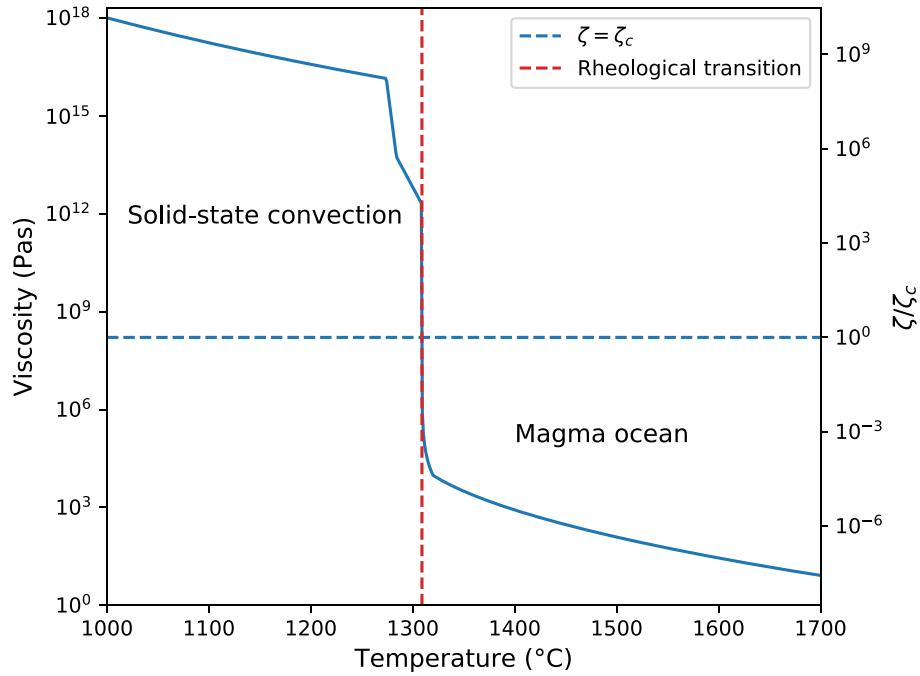

Figure 2. Viscosity function and corresponding Shields number taking into account the rheological transition, based on the crystallization series described in Figure B2. The rheological transition occurs for a solid fraction of $\phi = 60$vol%, which corresponds in our simplified three-mineral model to the temperature $T_{\mathrm{RT}} = 1307$°C. The viscosity function determines directly the Shields number (right-hand y axis), which is calculated here for a generic value of $Ra_H = 10^{20}$, and values from Table 1 (Equation 24). The horizontal dashed blue line stands for the critical value of the Shields number $\zeta = \zeta_c$.

To ensure the continuity of the viscosity at $\phi = \phi_{\mathrm{RT}}$, ϕ_c is adjusted to 60.0002% to get a viscosity at liquidus ≈10 Pa s (Rubie et al., 2003). The rheological transition described here is displayed in Figure 2 assuming batch melting, so that the temperature is a direct measure of the solid content ϕ given by Equation 30. Figure 2 shows that the viscosity decreases at the rheological transition by at least seven orders of magnitude. Beyond this transition, the silicate mantle behaves like a liquid suspension called "magma ocean," according to Taylor and Norman (1992).

2.4. Internal Magma Ocean, Core Formation, and Proto-Crust

Once the rheological transition is reached, two types of differentiation may occur: (a) metal-silicate segregation and (b) crystal/melt segregation in the remaining silicate magma ocean.

Here we assume for simplicity that core-mantle differentiation is total and occurs instantaneously at the rheological transition as the fluid becomes drastically less viscous (Höink et al., 2006). All the iron enters the core and mass conservation gives the following relationship between the ratio R_c/R and densities:

$$f_c = \frac{R_c}{R} = \left(\frac{\rho}{\rho_{\mathrm{Fe}}} x_{\mathrm{Fe}} \right)^{1/3}, \tag{12}$$

which yields $f_c = 0.44$ with values summarized in Table 1. Thus by assumption, all the ^{60}Fe enters the core, however ^{26}Al is partitioned into the silicate magma ocean.

In a material with a strongly temperature dependent viscosity, such as the silicates, convection takes place under a stagnant lid whose thickness is about 1 km (Appendix C). The conductive lid is an undifferentiated, solid layer preserved at the surface of the magma ocean, a classical hypothesis in the literature (Elkins-Tanton, Burgess, & Yin, 2011; Elkins-Tanton, Weiss, & Zuber, 2011; Haack & Rasmussen, 1990; Mandler & Elkins-Tanton, 2013), which is also adopted in the present model. This conductive lid should be largely undisrupted by convection and insulates the magma ocean which contains the radioactive heat source. This configuration leads to high

temperatures, which yield high degrees of partial melting at the base of the lid. Thus, the top of the lid is cold and 100% solid whereas the base of the lid behaves like a slurry. Therefore, the conductive lid thickness is controlled by the rheological temperature. Below the stagnant lid, the magma ocean is a convective liquid suspension from which crystals can potentially segregate according to their buoyancy to form a basal cumulate and/or a flotation crust, a major focus of our study.

2.5. Energy Budgets in the Presence of a Magma Ocean

Energy budgets in the whole-mantle magma ocean and the core lead to the following evolution equations for, respectively, the bulk average temperature of the magma ocean $T_{\rm MO}$ and of the core T_c:

$$\rho_{\rm Sil} c_{p,\rm Sil} \frac{{\rm d}T_{\rm MO}}{{\rm d}t} = H_{\rm MO} + Q_{\rm CMB} \frac{S_c}{V_m} - Q_s \frac{S_m}{V_m}, \tag{13}$$

$$\rho_{\rm Fe} c_{p,\rm Fe} \frac{{\rm d}T_c}{{\rm d}t} = H_c - Q_{\rm CMB} \frac{S_c}{V_c}, \tag{14}$$

where Q_s is the surface heat flux, $Q_{\rm CMB}$ is the heat flux at the core mantle boundary (CMB), H_i is the volumetric rate of internal heating in the layer i, $S_m = 4\pi R^2 (1 - \delta_{\rm L}/R)^2$ is the surface area of the magma ocean, $V_m = 4/3\pi R^3 \left[(1 - \delta_{\rm L}/R)^3 - (f_c + \delta_{\rm H}/R)^3\right]$ is the volume of the magma ocean, $S_c = 4\pi R^2 f_c^2$ is the surface of the core and $V_c = 4/3\pi R^3 f_c^3$ is its volume. Incorporated in the above equations is the possibility that crystals both heavier than and lighter than the melt may form. They can eventually sediment and form a cumulate at the CMB and a flotation crust of thickness $\delta_{\rm H}$ and $\delta_{\rm L}$ respectively.

The source of internal heat is twofold: (a) one part is due to energy supplied by radioactive decay, (b) the other part is due to latent heat absorbed during melting or released during crystallization. Assuming ^{60}Fe to be partitioned into the core and ^{26}Al into the silicate magma ocean, the radioactive heating rates are calculated by multiplying Equations 3 and 4 by a concentration factor:

$$H_{\rm Fe} = H_{0,\rm Fe}\, f_c^{-3}, \tag{15}$$

$$H_{\rm Al} = H_{0,\rm Al} \left[\left(1 - \frac{\delta_{\rm L}}{R}\right)^3 - \left(f_c + \frac{\delta_{\rm H}}{R}\right)^3 \right]^{-1}, \tag{16}$$

whereas the heat source associated with latent heat in each reservoir is:

$$H_{LH,\rm Fe} = -\frac{\rho_{\rm Fe} L_{\rm Fe}}{T_l^{\rm Fe} - T_s^{\rm Fe}} \frac{{\rm d}T_c}{{\rm d}t}, \tag{17}$$

$$H_{LH,\rm Sil} = -\frac{\rho_{\rm Sil} L_{\rm Sil}}{T_l^{\rm Sil} - T_s^{\rm Sil}} \frac{{\rm d}T_{\rm MO}}{{\rm d}t}, \tag{18}$$

We get the internal heating rate for the magma ocean and the core, respectively: $H_{\rm MO} = H_{\rm Al} + H_{LH,\rm Sil}$ and $H_c = H_{\rm Fe} + H_{LH,\rm Fe}$

The heat fluxes are expressed using the scaling laws for convection (Howard, 1964; Townsend, 1964). The surface heat flux is given by:

$$Q_s = k_{\rm Sil} \left(\frac{\alpha_{\rm Sil} \rho_{\rm Sil} g}{\kappa_{\rm Sil} \eta_{\rm Sil}} \right)^{1/3} \left(\frac{T_{\rm MO} - T_{\rm lid}}{C_T} \right)^{4/3}, \tag{19}$$

where $k_{\rm Sil}$ is the thermal conductivity of silicate, $g = 4/3\pi \mathcal{G} \rho R$ the surface acceleration of gravity, with $\mathcal{G}$ the gravitational constant, and $T_{\rm lid}$ is the temperature at the base of the crust. The temperature $T_{\rm lid}$ is determined by matching the conductive heat flux in the lid with the convective flux from the magma ocean, which yields:

$$Q_s = k_{\rm Sil} \frac{T_{\rm lid} - T_s}{\delta_L(t)} \frac{R(t)}{R(t) - \delta_L(t)}, \tag{20}$$

For the CMB heat flux, we consider the continuity of the temperature at the core/mantle interface and the heat flux from both sides. Two cases have to be considered. If the core is colder than the magma ocean, the temperature $T_{b,\mathrm{MO}}$ is determined assuming conductive heat transfer in the cumulate and the core to be isothermal, at temperature T_c, which yields:

$$Q_{\mathrm{CMB}} = k_{\mathrm{Sil}} \frac{T_{b,\mathrm{MO}} - T_c}{\delta_H(t)} \frac{R_c(t) + \delta_H(t)}{R_c(t)}. \tag{21}$$

If the magma ocean is colder than the core, both reservoirs convect. We consider a TBL at the top of the core, beyond the cumulate whose basal temperature is $T_{b,\mathrm{CMB}}$. In this case, the CMB heat flux is given by the scaling law for convection in the core:

$$Q_{\mathrm{CMB}} = k_{\mathrm{Fe}} \left(\frac{\alpha_{\mathrm{Fe}} \rho_{\mathrm{Fe}} g_c}{\kappa_{\mathrm{Fe}} \eta_{\mathrm{Fe}}} \right)^{1/3} \left(\frac{T_c - T_{b,\mathrm{CMB}}}{C_T} \right)^{4/3}, \tag{22}$$

and $T_{b,\mathrm{CMB}}$ is deduced by assuming conductive heat transfer through the cumulate and a top temperature equal to that of the magma ocean, which yields:

$$Q_{\mathrm{CMB}} = k_{\mathrm{Sil}} \frac{T_{b,\mathrm{CMB}} - T_{\mathrm{MO}}}{\delta_H(t)} \frac{R_c(t) + \delta_H(t)}{R_c(t)}. \tag{23}$$

The solution of this set of equations relies on the knowledge of two parameters: the thickness of the flotation crust δ_L and the thickness of the basal cumulate δ_H. These two thicknesses can be obtained using the scaling laws for crystal deposition established in the companion paper (Sturtz, Limare, Kaminski, & Tait, 2022).

2.6. Mass Conservation and Evolution of Crystal Deposits

The magma ocean contains a total volume of solid crystals ϕ_0 that depends on the temperature and initial composition as discussed in the following section (Section 3, Equation 30). The possibility to sustain crystals in suspension and/or to form deposits is controlled by a criterion based on a dimensionless parameter, the Shields number, that compares the convective shear stress and the buoyancy of crystals (Sturtz et al., 2021). For a magma ocean that is already iron depleted, the Shields number is:

$$\zeta_{\mathrm{MO}} = \frac{\eta_{\mathrm{Sil}} \kappa_{\mathrm{Sil}}}{\Delta \rho g r h_{MO}^2} \left(Ra^*_{H,\mathrm{Sil}} \right)^{3/8}, \tag{24}$$

with Ra^*_H the modified Rayleigh-Roberts number for a time-varying system:

$$Ra^*_{H,\mathrm{MO}} = \frac{\alpha_{\mathrm{Sil}} \rho_{\mathrm{Sil}} g H^* h_{\mathrm{MO}}^5}{\kappa_{\mathrm{Sil}} \eta_{\mathrm{Sil}} k_{\mathrm{Sil}}}, \tag{25}$$

with H^* the effective heating rate given by:

$$H^* = H_{\mathrm{Sil}} - \rho_{\mathrm{Sil}} c_{p,\mathrm{Sil}} \frac{\mathrm{d}T_{\mathrm{MO}}}{\mathrm{d}t}, \tag{26}$$

and h_{MO} the thickness of the magma ocean:

$$h_{\mathrm{MO}} = (1 - f_c)\ R - \delta_{\mathrm{L}}(t) - \delta_{\mathrm{H}}(t). \tag{27}$$

If ζ_{MO} is larger than the critical value $\zeta_c = 0.29 \pm 0.17$, the convective vigor is large enough to destabilize any cumulate previously formed and to prevent suspended crystals from settling and/or floating. But if $\zeta_{\mathrm{MO}} < \zeta_c$, the buoyancy of crystals is large enough that they segregate from the liquid suspension and form a basal cumulate and/or a flotation crust. The sharp variation of viscosity that occurs at the rheological transition makes η the key parameter for the segregation of crystals as $\zeta_{\mathrm{MO}} \sim \eta^{5/8}$. As illustrated in Figure 2, segregation of particles is possible in the magma ocean episode, and deposits previously formed are preserved as convective shear stress is too low to erode them. Even if convection is turbulent (very high Rayleigh-Roberts number), the viscosity is so small that the Shields number will never reach the critical value, hence crystal layers will be always stable, and potentially growing.

Table 2
Characteristics of the Silicate Mantle With a Mass Composition of 60/20/20 of Forsterite/Diopside/Anorthite

	Forsterite	Anorthite	Diopside
Liquidus temperature (°C)	1,700	1,320	1,280
Solidus temperature (°C)	1,270	1,270	1,270
$\Delta\rho$ (kg m^{-3})	400	−50	400

Note. $\Delta\rho$ stands for the average density contrast between the liquid and the considered solid phase.

The evolution of the thickness of both layers δ_i is given by the deposition law described in the companion paper (Sturtz, Limare, Kaminski, & Tait, 2022):

$$\frac{\mathrm{d}\delta_i}{\mathrm{d}t} = c_d v_s \frac{\overline{\phi}_{i,\mathrm{sus}}}{\phi_{\mathrm{RLP}}}. \tag{28}$$

where v_s is the settling velocity, c_d is a constant, $\phi_{i,\mathrm{sus}}$ the volume fraction of crystal i in suspension that contributes to the thickening of the corresponding deposit, and ϕ_{RLP} is the packing inside the deposit. The volume fraction of crystals that remains in suspension is given by mass conservation as explained in Appendix D.

Experimentally, Sturtz, Limare, Kaminski, and Tait (2022) pointed out that the sedimentation velocity v_s in the presence of convection scales with the Stokes velocity of particles, with $c_d = 0.24 \pm 0.14$ close to the 2/9 coefficient of the Stokes velocity. This reasoning is consistent with a dilute suspension. We adapted this model by using the complete rheological law described previously and thus settling velocity of crystal i is given by:

$$v_{s,i} = \frac{\Delta\rho_i g r_i^2}{\eta(T,\phi)}, \tag{29}$$

with $\eta(T, \phi)$ described in Section 2.3.

3. Magma Ocean Dynamics—Crystal/Melt Segregation in an Early Accreted Planetesimal

3.1. Mineralogic Composition of the Silicate Mantle

We used a simplified phase diagram in the calculation of thermal and compositional evolution of mantle and in the computation of liquid density as a function of composition and temperature. The silicate system is considered as being Fe and Na free and therefore represented by the ternary system Forsterite-Anorthite-Diopside (Appendix B, Figure B1). The volume content of each type of crystal is given by:

$$\phi = \phi_{\mathrm{Fo},cr} + \phi_{\mathrm{An},cr} + \phi_{\mathrm{Di},cr}, \tag{30}$$

$$\phi_{i,cr} = \phi_{i,0} \frac{T_l^i - T}{T_l^i - T_s^i}, \tag{31}$$

with $\phi_{i,0}$ the total volume content of the component i, $\phi_{i,cr}$ the volume fraction of the component i that crystallizes, T_l^i and T_s^i the liquidus and solidus temperatures of the component i.

As we aim to study the sedimentation process occurring in a magma ocean, we have to constrain the density contrast between the liquid silicate and the crystals. We considered a typical composition of mass content 60/20/20 forsterite/diopside/anorthite. We calculated the melt density for each mantle mineral component (forsterite/diopside/anorthite) by using molar volume data for each individual oxide and their respective molar fraction (Niu & Batiza, 1991). We took into account the temperature dependence of the partial molar volume, whereas the pressure effect was neglected. The density during crystallization is shown in Figures B2b and B2c. Table 2 contains the averaged values of the density contrasts that fed the model. Forsterite and diopside crystals are both negatively buoyant with a similar density contrast of about $\Delta\rho_H = 400$ kg m^{-3} whereas the anorthite crystals are slightly positively buoyant ($\Delta\rho_L = -50$ kg m^{-3}).

3.2. Typical Evolution of a Planetesimal Structure

We first apply the model presented above to a planetesimal of radius $R = 270$ km. We consider a crystal size of 0.5 mm and data from Table 2. Figure 3a shows the evolution of the internal structure. After a short episode of conductive regime spanning from 0 to 0.36 Myr, the rheological transition is reached and the magma ocean

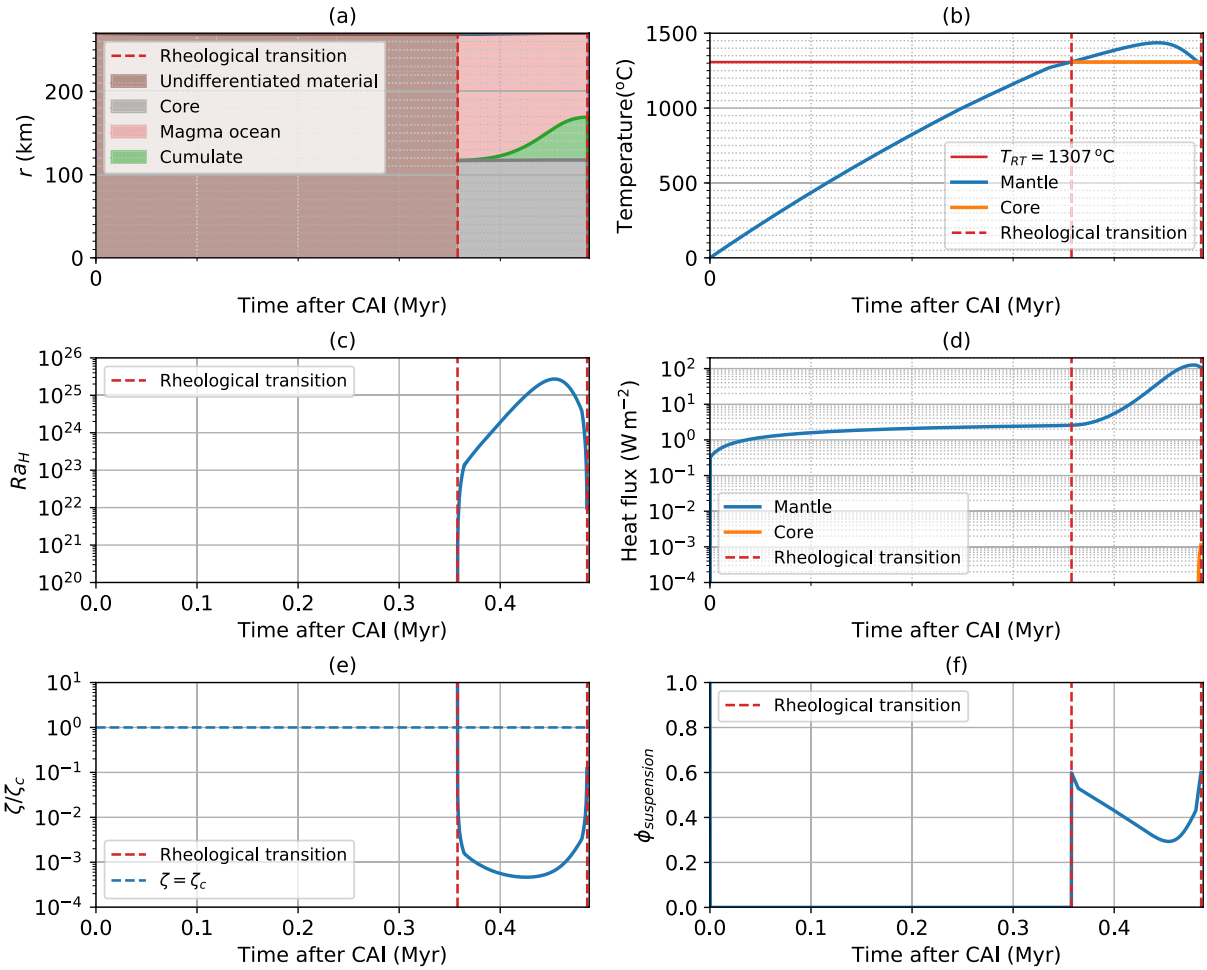

Figure 3. The case of a 270 km planetesimal with the silicate composition of 60/20/20 Fo/Di/An ($\Delta\rho_H = 400$ kg m^{-3}, $\Delta\rho_L = -50$ kg m^{-3}), accreted instantaneously at $t_0 = 0$ Myr. (a) Evolution of the radial structure, (b) temperatures of the magma ocean and the core, (c) Rayleigh-Roberts number, (d) heat flux out of the mantle and the core, (e) Shields number, (f) suspended crystal fraction. Crystal size: $r = 0.5$ mm.

episode begins with 60 vol% of crystals in suspension. Although the Rayleigh-Roberts number is supra-critical (Figure 3c), there is no solid-state convection stage between the conduction one and the full-internal magma ocean one, due to the convection onset delay, Equation C2. During magma ocean stage, the Shields number in the magma ocean is far below the critical value (Figure 3e), and crystals can settle as a basal cumulate or a flotation crust according to their buoyancy. Between 0.36 and 0.49 Myr the volume fraction of crystals (Figure 3f) decreases because (a) a cumulate of forsterite forms at the base of the magma ocean and (b) the temperature in the magma ocean rises (Figure 3b) due to the combined effect of radioactive heating and the thermal insulation of the chondritic crust (Figure 3b). When settling becomes slower than the crystallization rate the volume fraction of crystals in the magma ocean increases until the rheological transition is reached, at 0.49 Myr. At this time, the planetesimal is composed of a thin undifferentiated crust (<1 km), overlying a 100 km-thick well-mixed interior composed of the slightly positively buoyant minerals (anorthite), the entire quantity of diopside and the remaining forsterite that have not settled. A 52 km thick cumulate composed of forsterite formed at the CMB, covering a 118 km thick metallic core (Figure 4a). In this figure, we neglected the melt still present in the cumulate due to inefficient melt migration, which is clearly an approximation. This residual melt will crystallize during the next step of the thermal evolution, that is, the solid state convection regime. The density contrast between the well mixed layer and the forsterite cumulate is relatively important so this heterogeneity is likely to be preserved at the end of the solid state convection episode.

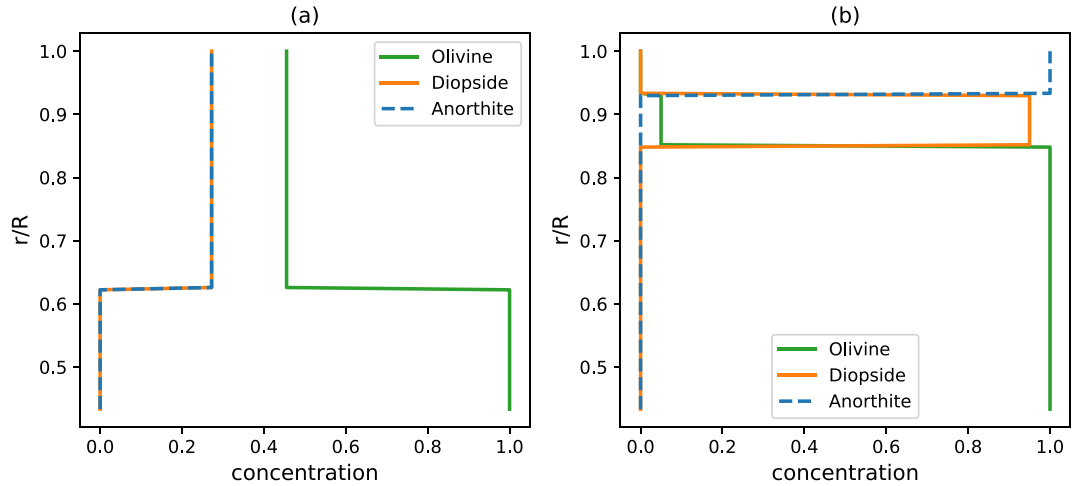

Figure 4. Composition as a function of relative radius in the case of a planetesimal with the silicate composition of 60/20/20 Fo/Di/An ($\Delta\rho_H = 400$ kg m^{-3}, $\Delta\rho_L = -50$ kg m^{-3}), accreted instantaneously at $t_0 = 0$ Myr. (a) Crystal size: $r = 0.5$ mm, (b) Crystal size: $r = 2$ mm.

In this case, anorthite crystals did not settle before the end of the magma ocean episode for their deposition time is longer than the magma ocean lifetime. This is due to the small density contrast between the anorthite and the melt, which is fixed by the initial composition, and to the small crystal size considered.

3.3. Influence of Crystal Size

We modeled the internal structure of the mantle of a 270 km radius planetesimal with a much larger crystal size (2 mm), and the results are shown in Figure 5. The early stage of the magma ocean episode is similar to the one described in the previous case: the rheological transition is reached at 0.36 Myr, metal/silicate segregation occurs and a magma ocean forms in the volume delimited by the ∼km size thick undifferentiated crust and the core. Heavy forsterite crystals first settle and then melt as the temperature rises in the magma ocean due to radioactive heating. Once the magma ocean starts to cool ($t > 0.45$ Myr), crystals form in the magma ocean and the cumulate thickens. Anorthite starts to crystallize, and light crystals begin to float, settling at the base of the primordial crust. Crust thickening strengthens the thermal insulation of the magma ocean and diminishes the surface heat losses (Figure 5d). This slows down the cooling of the magma ocean and consequently increases its lifetime. Magma ocean temperature is buffered just above the value of the rheological transition temperature, whose value changes with the composition of the liquid-like mantle situated above the cumulate (Figure 5b). Magma ocean ends at ≈6.4 Myr, considerably later than in the previous case, in the absence of the flotation crust (0.49 Myr). The rheological transition temperature at the end of the magma ocean is close to the silicate solidus, since in this case, all the crystals have enough time to deposit (Figure 5f). For compositions that make possible the deposition of light crystals and the building of a floating lid, the timescale of the magma ocean episode can be considerably large (between 2 and 9 Myr) and becomes compatible with effective melt migration and compaction of cumulates (Appendix A, Figure A1a). The volume of cumulate and of the flotation lid are likely to be free of melt. The typical composition in each layer of this well segregated mantle is shown in Figure 4b.

To better illustrate the effect of the crystal size, we examine the structure of the planetesimal at the end of the magma ocean episode for different values of crystal radius r spanning from 0.1 to 5 mm. We displayed the thickness of the metallic core, the cumulate, the well-mixed interior, and the crust in Figure 6a. For small crystal size (between 0.1 and 0.6 mm), a significant quantity of crystals remains in suspension in the magma ocean and the planetesimal mantle is essentially composed of a cumulate of forsterite and a well-mixed upper mantle composed of forsterite, diopside and anorthite. The larger the crystals, the thicker the forsterite cumulate, but the upper part of the mantle stays well-mixed. For $r > 0.62$ mm anorthite crystals are able to settle at the base of the chondritic, primordial crust, so the heat flow at the surface is reduced, the lifetime of the magma ocean is enhanced, so crystal segregation is complete. Two types of structures are therefore possible: one with a well-mixed upper mantle, and the second one similar to an "onion shell" with highly segregated layers, as illustrated in Figure 4. These two

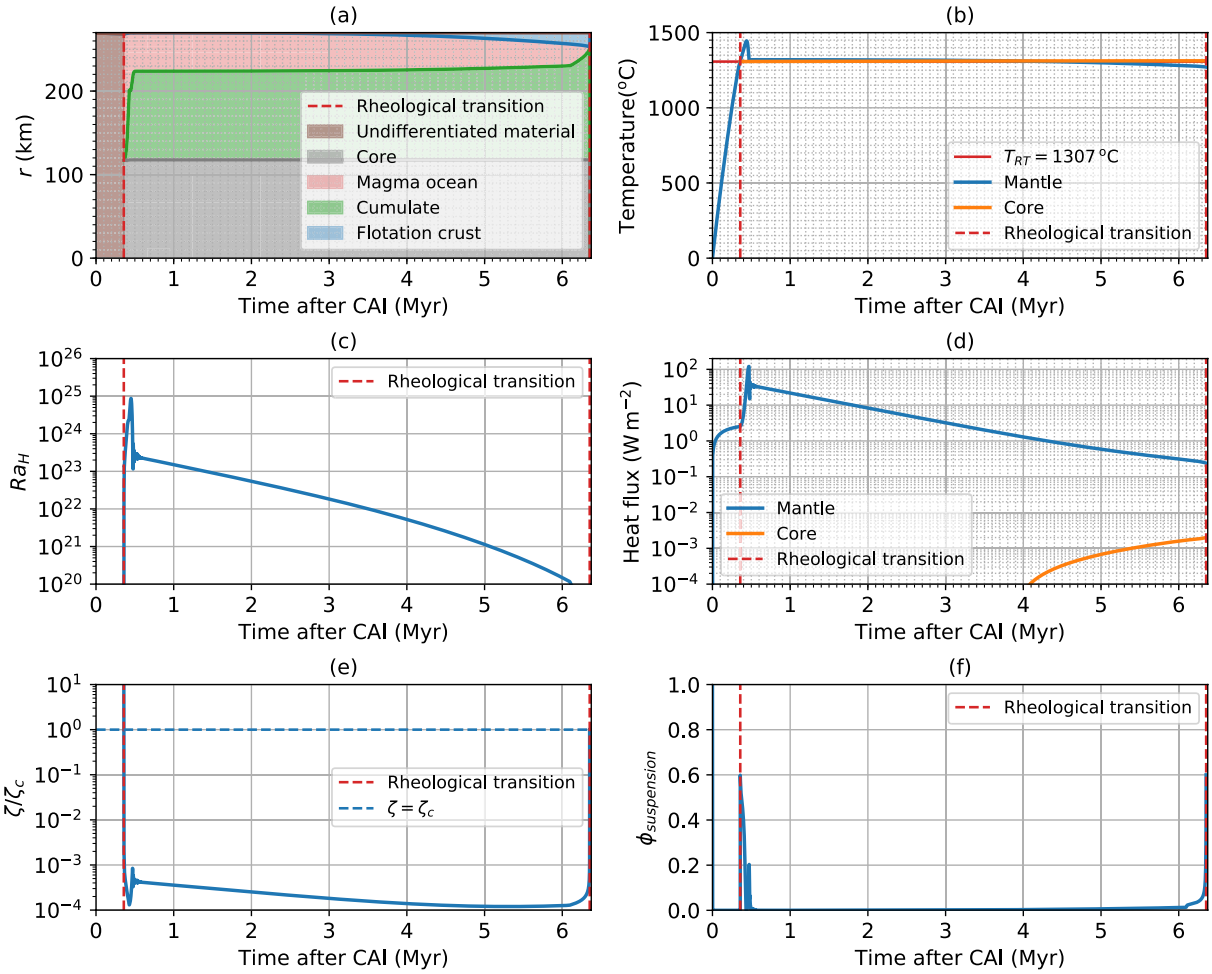

Figure 5. The case of a 270 km planetesimal with the silicate composition of 60/20/20 Fo/Di/An ($\Delta\rho_H = 400$ kg m^{-3}, $\Delta\rho_L = -50$ kg m^{-3}), accreted instantaneously at $t_0 = 0$ Myr. (a) Evolution of the radial structure, (b) temperatures of the magma ocean and the core, (c) Rayleigh-Roberts number, (d) heat flux out of the mantle and the core, (e) Shields number, (f) suspended crystal fraction. Crystal size: $r = 2$ mm.

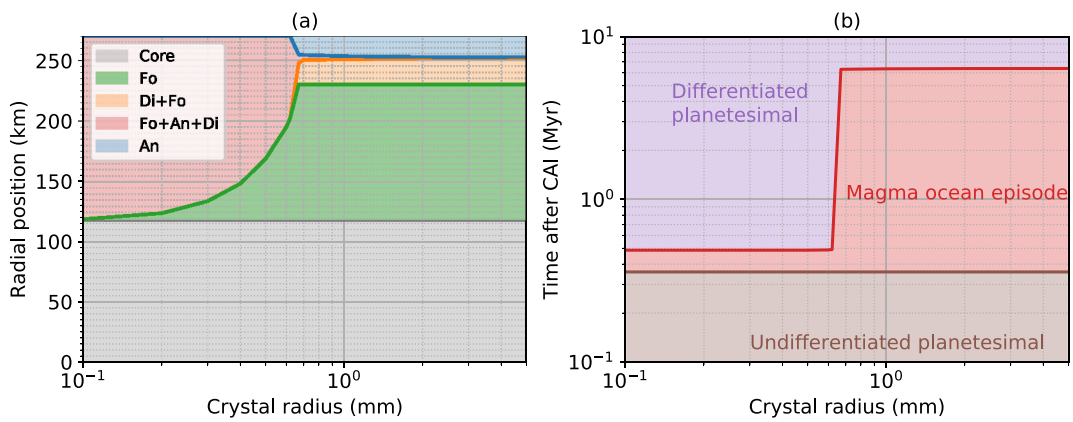

Figure 6. Sensitivity study showing the influence of the crystal radius on the final structure of the mantle at the end of the magma ocean episode (a) the composition of the solid phase at the end of the magma ocean and (b) the duration of the magma ocean. Calculations are made for a 270 km radius planetesimal with the following crystal properties: $\Delta\rho_H = 400$ kg m^{-3}, $\Delta\rho_L = -50$ kg m^{-3}.

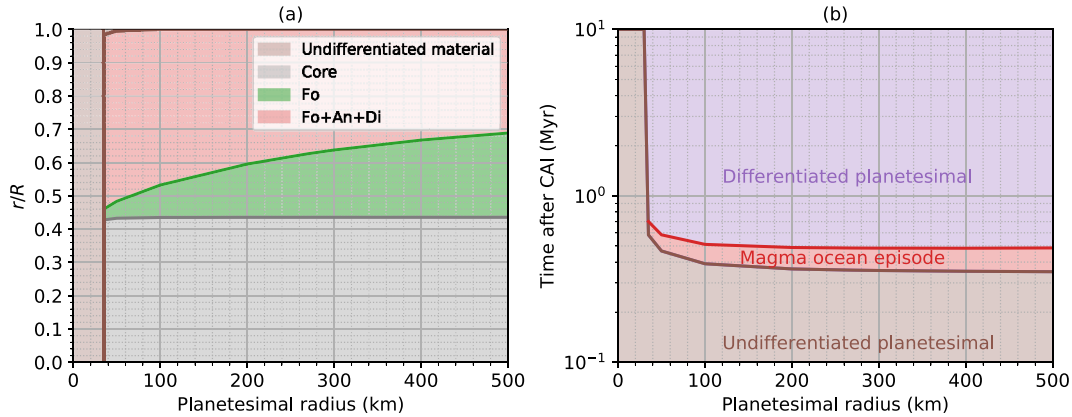

Figure 7. Sensitivity study showing the influence of the planetesimal radius on the final structure of the mantle at the end of the magma ocean episode. (a) The composition of the solid phase at the end of the magma ocean and (b) the duration of the magma ocean. Crystal properties are: $\Delta\rho_H = 400$ kg m^{-3}, $\Delta\rho_L = -50$ kg m^{-3}, $r = 0.5$ mm.

types of structure are associated with two discrete values of the magma ocean lifetime; each of them independent of the crystal size (Figure 6b). The transition between them is sharp and depends essentially on the sedimentation velocity (i.e., size and density contrast) of the light crystals, if any.

3.4. Influence of Planetesimal Radius

We tested the sensitivity of our model with respect to the planetesimal radius for two cases corresponding to the two types of structure documented in the previous section: incomplete segregation defined by small size crystals (0.5 mm) and complete segregation defined by large size crystals (2 mm). The other crystal properties are fixed ($\Delta\rho_H = 400$ kg m^{-3}, $\Delta\rho_L = -50$ kg m^{-3}). Results obtained in the case of incomplete segregation defined by small size crystals (0.5 mm) are shown in Figure 7. Again, we examine the structure of the planetesimal at the end of the magma ocean episode: Figure 7a, and the duration of the magma ocean episode: Figure 7b. For 30 km $< R <$ 100 km, there is a slightly thicker chondritic, primordial crust that causes a delay in both the beginning and the end the magma ocean. The relative thickness of the cumulate increases with the planetesimal size, depending on the relative importance of the timing of crystal deposition and of magma ocean cooling. The transition between the domain where only a cumulate exists to the 'onion-shell" structure depends on the planetesimal radius, occurring at slightly lower crystal radius (e.g., $r = 0.5$ mm for $R = 500$ km and $r = 0.9$ mm for $R = 100$ km).

Results obtained in the case of complete segregation defined by large size crystals (2 mm) are shown in Figure 8. Figure 8a shows that the "onion-shell" structure of a differentiated mantle is the essentially the same regardless of planetesimal size, with a slightly thicker chondritic crust at small values of planetesimal radius. Figure 8b shows that the same relative crust thickness has a stronger influence on planetesimals of large radius, since cooling is proportional to the surface over volume ratio, therefore inversely proportional with the planetesimal radius. Larger bodies have a longer magma ocean episode.

4. The Case of Vesta

The asteroid 4 Vesta is a 267 km radius rocky differentiated body orbiting in the asteroid belt, and considered to be an almost intact pristine protoplanet (Consolmagno et al., 2015). Vesta is thought to be the parent body of over 2,000 achondrite meteorites called the HED series (howardite-eucrite-diogenite) (McSween et al., 2013). Diogenites are cumulates, that is, their bulk compositions (in this case harzburgite, pyroxenite) are far more refractory than known silicate liquid compositions, whereas eucrites are igneous rocks whose bulk compositions are much closer to known magma compositions. Cumulate compositions are commonly attributed to mechanical processes, often heaped under the label of fractional crystallization (Zuber et al., 2011). Howardites are brecciated basalts and pyroxenites, and correspond compositionally to a mixture of eucrites and diogenites. Meteoritic data indicate that the eucrite/diogenite mass ratio is 2:1 (McSween et al., 2013, 2019).

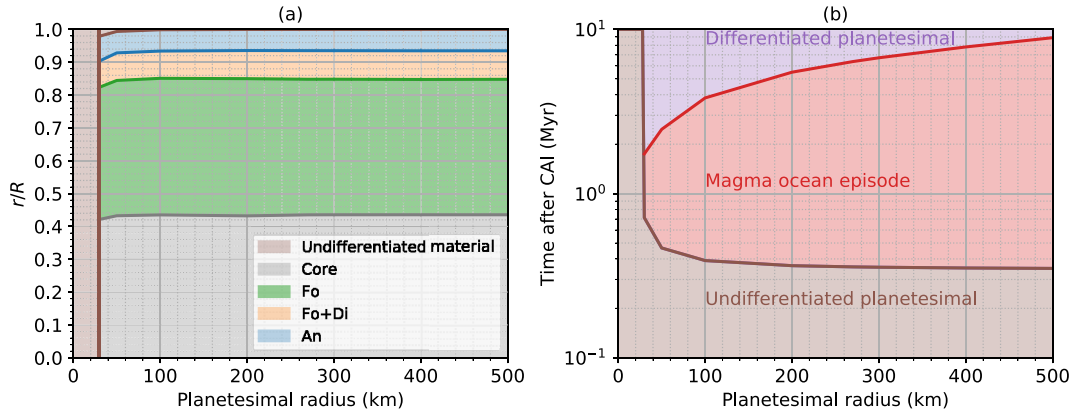

Figure 8. Sensitivity study showing the influence of the planetesimal radius on the final structure of the mantle at the end of the magma ocean episode. (a) The composition of the solid phase at the end of the magma ocean and (b) the duration of the magma ocean. Crystal properties: $\Delta\rho_H = 400$ kg m^{-3}, $\Delta\rho_L = -50$ kg m^{-3}, $r = 2$ mm.

Crystallization models in the literature predict a layered structure of Vesta with an eucritic upper mantle, sometimes also called eucritic crust and a basal dunitic/harzburgitic cumulate. Depending on the model considered, diogenites could either result from the late crystallization of the remaining magma ocean between the eucritic crust and the cumulate (Righter & Drake, 1997), or could correspond to plutonic layers in the eucritic crust (Mandler & Elkins-Tanton, 2013). A third type of scenario involves the crystallization of a shallow magma layer above a depleted lower mantle with a melt content bellow the rheological transition, which could arise if ^{26}Al-rich melt migrates efficiently to the surface, on a time-scale comparable with or shorter than the decay half-life (Neumann et al., 2014). These predictions have been compared to the observations of the Dawn mission (Russell et al., 2013). The petrologic complexity mapped on Vesta is consistent with HEDs but did not establish unambiguously evidence against or in favor of a full internal magma ocean (McSween et al., 2013).

Two major craters (Rheasilvia and Veneneia) are located in the southern hemisphere (Jaumann et al., 2012; Marchi et al., 2012). Impact models predict that the impacts that formed these craters induced an excavation depth of 60–100 km (Clenet et al., 2014). The Vestean mantle, and thus according to previous crystallization models, diogenites and even olivine-rich cumulates, should have been exposed. However, Dawn data only identified eucritic and howarditic material at the surface (De Sanctis et al., 2012), and diogenites are not clearly detected (McSween et al., 2019). Several hypotheses have been formulated to explain the inconsistency between petrological models and Dawn observations. First, it has been pointed out that the eucritic layer might be potentially very thick (60–100 km), explaining why excavations did not unveil diogenites. But diogenite and olivine are, however, potentially present as plutonic patches and could correspond to density anomalies measured during the Dawn mission (Clenet et al., 2014; Mandler & Elkins-Tanton, 2013; McSween et al., 2019). Another hypothesis is to rely on the mechanical mixing associated with impacts that could have caused the homogenization of the outer 100 km of Vesta (Jutzi et al., 2013).

We used our model to reconstruct a thermal evolution for Vesta based on the hypothesis of an early whole-mantle magma ocean as argued earlier. In the previous section, we described in detail the evolution of a planetesimal with a radius of 270 km that represents the possible evolution of Vesta in the hypothesis that it accreted early (Figure 3). A magma ocean forms at 0.36 Myr and triggers the formation of a 118-km radius metallic core, a size that is consistent with the estimates based on data from Dawn (Russell et al., 2013). Then, crystallization starts with olivine and crystal-melt segregation producing an olivine-rich heavy cumulate at the CMB. At the end of the magma ocean's life, if crystals are small enough, the sedimentation is incomplete and a well-mixed upper mantle is preserved (Figure 6). This layer is enriched in anorthite and diopside, and depleted in forsterite. We propose that the Rheasilvia crater that excavated 60–100 km of the vestean mantle (r/R between 0.78 and 0.63) would have excavated this well-mixed interior, but would not have attained the deeper olivine cumulates. Figure 3a shows that a well mixed interior of 100 km would imply a crystal radius $r < 0.5$ mm. The crystal size lower limit is imposed by the olivine concentration of the depleted mantle above the cumulate. According to McSween et al. (2013), the olivine content should be below the detection limit of spectral measurements delivered by Dawn mission (<30% in the presence of abundant orthopyroxene). Figure 4a ($r = 0.5$ mm), shows that

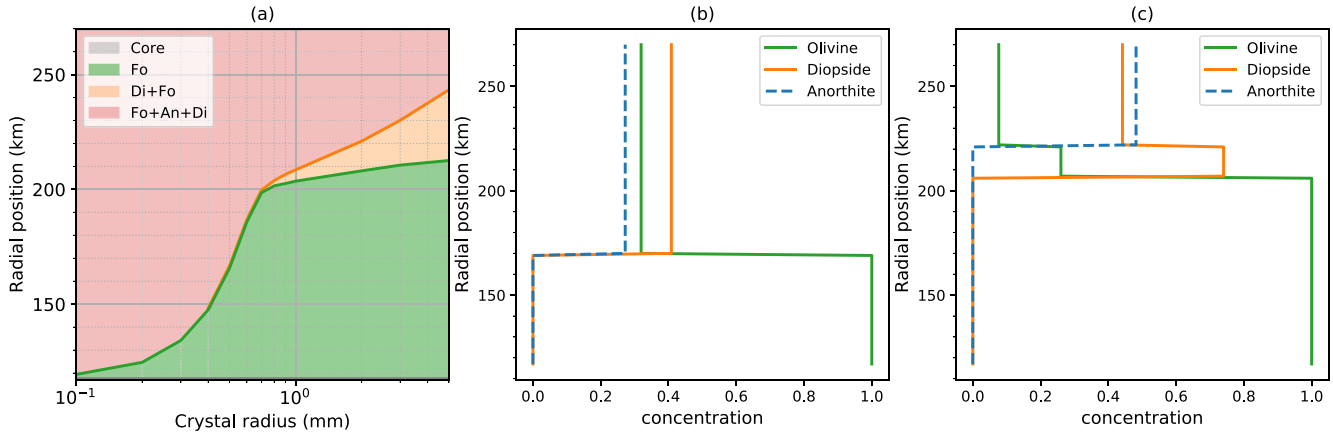

Figure 9. The case of a 270 km planetesimal with the silicate composition of 50/30/20 Fo/Di/An ($\Delta\rho_H = 400$ kg m^{-3}, $\Delta\rho_L = 0$ kg m^{-3}), accreted instantaneously at $t_0 = 0$ Myr. (a) Radial structure as a function of the crystal radius. (b) Radial composition for crystal size: $r = 0.5$ mm. (c) Radial composition for crystal size: $r = 2$ mm.

the olivine composition for a relative radius r/R larger than 0.63 (equivalent to an excavation depth of 100 km) would imply an olivine concentration of about 40%, which is above the detection threshold of Dawn mission. Therefore either the excavation depth is smaller than 100 km, or the initial olivine concentration should be less than predicted by chondritic models, as already underlined by Clenet et al. (2014). For the initial concentration considered up to now (60/20/20 Fo/Di/An), a 60 km excavation depth with an olivine concentration at the limit of detection is compatible with a crystal radius $r = 0.62$ mm, which is the value of crystal size at the interface between the two types of structure in Figure 6a. For larger values of the crystal size $r > 0.62$ mm, the structure of the planetesimal would be highly segregated (Figure 4b) that would expose an olivine layer for an excavation depth larger than 40 km.

In the following we explored the possibility that the initial olivine concentration is lower than the case considered up to now: 50/30/20 Fo/Di/An. The resulting density contrasts are shown in Figure B3, olivine and diopside have a similar, large density contrast, and anorthite crystals are neutrally buoyant. We investigated the role of the crystal size on the radial structure (Figure 9a). A crystal size of $r = 0.5$ mm (Figure 9b) would produce a cumulate and an upper mantle with a 100 km thickness compatible with a depleted mantle with an olivine content <30%. Larger values of crystal size lead to a much thicker olivine cumulate layer and hence are only compatible with an excavation depth of the order of 60 km, but this would imply the exposure of a layer containing a considerable amount of diopside (75%), which was not detected. Therefore a well mixed mantle of 60–100 km thickness above a pure olivine cumulate is compatible with a crystal size of the order 0.5–1 mm if the initial olivine content is in the range 50%–60%. These observations further highlight the importance of grain size in influencing the body's internal structure.

5. Discussion

A magma ocean episode is a very important way to favor crystal-melt segregation, as the viscosity is reduced so that the Shields number becomes subcritical, inducing internal layering. The layered structure that can form is thus intimately linked to the segregation processes that occur during the magma ocean episode. We studied the sensitivity of this structure with respect to two main parameters: (a) the crystal radius r which is the most important parameter that promotes sedimentation, (b) the planetesimal radius R, as it constrains the surface over volume ratio and therefore the cooling of the body, which is a trade-off between the heat lost at the surface and the heat released by radioactivity. One striking feature of the results presented is that changing the grain size by a small amount, in the sub-millimeter range, has a substantial effect on the final large-scale internal structure of a silicate planetesimals. If light crystals can form and settle, they may contribute to the thickening of the crust, accentuating the thermal insulation of the magma ocean and therefore affecting the thermal history of the planetesimal. However this latter effect may not have been important in Vesta's evolution.

Our model contains a certain number of simplifications. First of all we assumed batch melting: that is, no melt migration during partial melting. If melt migration occurs efficiently during partial melting, the radioactive heat

source (^{26}Al) could be concentrated near the surface, and as a result a whole-mantle magma ocean may not develop. We adopted the internal magma ocean scenario since for early accreted planetesimals, melt segregation is likely to be slower that melting by heating: the heat source is large enough to produce high degrees of melt and the grain sizes reported from chondritic meteorites by Simon et al. (2018) are small enough to suggest that after the planetesimal has formed, melt segregation is not likely to be efficient.

Once a magma ocean has formed, the degree of crystal segregation is a trade-off between the dynamics of crystal deposition and of cooling. Two parameters controlling the deposition dynamics were considered as being constant: the density contrast and the viscosity of the liquid silicate. The density contrast is fixed by the composition of silicate supposed to be iron free, which is a good approximation in very reduced conditions. When both MgO and FeO components are present, MgO is more compatible than FeO in the olivine crystals compared with the liquid (Roeder & Emslie, 1970). All else being equal, replacing some MgO with FeO in the liquid phase will tend to augment the latter's density. The influence of FeO on the iron-free system that we have considered until now, will imply that any positive buoyancy for plagioclase would be enhanced. The reduction in the density difference between olivine and melt would have a negligible effect as this is already very large. Therefore the presence of iron in the silicate mantle would, all else being equal, favor the occurrence of a flotation lid, with the already mentioned increase of magma ocean lifetime and the degree of crystal segregation.

We did not consider the eventual effect that a stable density stratification might arise in the upper thermal boundary layer of the magma ocean if crystals form there and are removed by sedimentation at a rate faster than the time scale of convective instability. This effect is subtle and not easy to assess quantitatively as it requires detailed analysis of crystal nucleation and growth within the boundary layer simultaneous with convective instability of the layer. We note however, that such a density stratification would imply suppression of convective flow and therefore a dramatic reduction of the heat flux. The temperature would start to increase, so the crystal fraction would diminish, increasing the convective vigor. This negative feedback likely keeps the magma ocean temperature just above the rheological transition temperature in a convective regime.

We neglected the contribution of crystal density contrast to the overall density of the upper boundary layer and hence to its convective instability, which can be incorporated by using an effective thermal expansivity. We did, however, test its influence on the Rayleigh number and on the surface heat flux. We estimated an effective thermal expansion coefficient for the liquid suspension up to one order of magnitude larger than the value of thermal expansion of the pure liquid. Since the Rayleigh number is already so large in the magma ocean regime, this would imply a negligible variation of the maximum heat flux and of the magma ocean lifetime.

We used an idealized viscosity function that assumes constant melt viscosity regardless of melt composition, which is not the commonly used model rheologies (Costa et al., 2009; Giordano et al., 2008). We used arbitrary reference values of viscosity: $\eta_0 = 10^{18}$ Pa s at 1000°C, and $\eta_l = 10$ Pa s at 1700°C, and we ensured the continuity of the viscosity function between these two values by adjusting the value of ϕ_c in Equation 11. The resulting structure is similar for larger values of η_0, for example, 10^{21} Pa s, provided that the value of the viscosity at the liquidus was kept low, that is, by re-adjusting the value of ϕ_c. The output of the model is essentially the same for values of η_l up 10^3 Pa s. Above this value, a flotation crust can be obtained only if unrealistic values of crystal size and density contrasts are being considered.

Although the compaction time scale is large, it can be comparable to the duration of the magma ocean in some cases, for example, when a floating lid is present. In this case we can consider the volumes of cumulate and floating lid to be free of melt. Otherwise, for short lifetime magma oceans this is likely to be inaccurate. Grain size is once again a key control parameter when assessing compaction time scale. Our model needs to be extended to take explicitly into account compaction and melt migration in order to provide a more quantitative explanation of complex petrological features in asteroids.

6. Conclusion

We develop a model for erosion/deposition of an erodible bed, and we adapt the Shields' formalism to study the evolution of magma oceans in planetary systems. This formalism is incorporated in a generic heat transport model enabling us to establish, with a proper choice of reference parameters, a likely evolution for early accreted planetesimals. To form basal cumulates and/or flotation crusts, planetesimals must have undergone a whole-mantle internal magma ocean episode, which happens for planetesimal radii larger than $R > 30$ km,

provided they accreted early. Beyond the rheological transition that marks the onset of the magma ocean episode, the mantle is a liquid suspension that convects under the relic of the stagnant lid that is a km-size proto-crust that insulates the magma ocean. Because heat is produced by radioactivity in the magma ocean, and as the crust acts like a thermal insulator, the temperature rises in the magma ocean well above the solidus. The temperature at the base of the stagnant lid stabilizes at the rheological temperature and the magma ocean temperature is buffered just above this value. After a 1–8 Myr magma ocean episode, the mantle reaches the rheological transition again and reverts back to a solid-state convection regime.

Two types of large scale mantle structure can be produced as a function of the crystal properties. For small crystal sizes, a magma ocean favors the appearance of layer of well-mixed mantle on top of an olivine cumulate. If the initial composition allows for the crystallization of minerals lighter than the melt, such as plagioclase, crystal sizes above a threshold value are necessary to produce a floating crust that will enhance the lifetime of the magma ocean and will therefore allow more efficient segregation. The result will be a highly heterogeneous "onion shell" structure, that could survive the last (and short) dynamical episode of solid state convection.

The model could be adapted to study magma oceans formed in larger bodies and produced by giant impacts. The layered structure produced during the magma ocean episode sets the initial conditions for the subsequent solid state convection in planetary mantles. The relics of this structure could be related to preserved heterogeneities for example,: in the Earth (Large low-shear-velocity provinces or Ultralow velocity zones) or in the Moon (KREEP basalts).

Appendix A: Melt Migration by Porous Flow

Melt velocities in Figure A1a were calculated according to McKenzie (1984):

$$u = \frac{k_\phi \Delta \rho g}{\phi_l \eta_l}, \tag{A1}$$

with the permeability k_ϕ depending on the melt fraction ϕ_l as follows:

$$k_\phi = \frac{r^2}{b} \frac{{\phi_l}^n}{(1-\phi_l)^m}, \tag{A2}$$

with constants n, m, and b equal to 3,2 and 200, respectively.

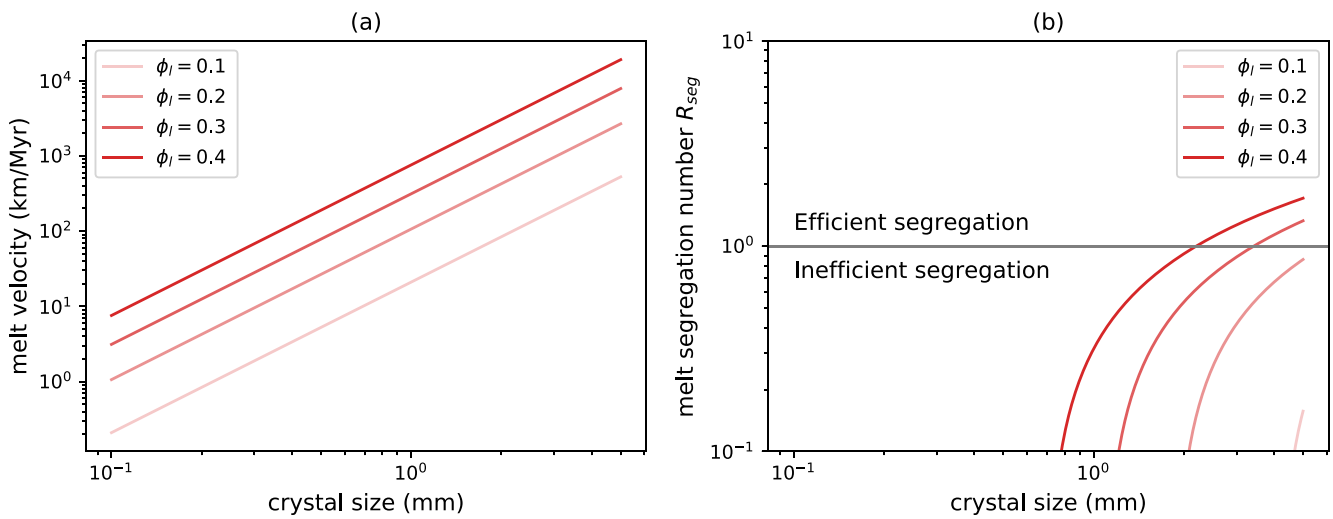

Figure A1. (a) Melt migration velocity and (b) segregation number as a function of crystal radius for different values of melt fraction $\phi_l = 1 - \phi_s$. The reference parameters are taken from Tables 1 and 2. The planetesimal radius is $R = 270$ km.

Batch melting due to internal heating occurs on a time scale of the order of the radioactive halftime sufficient to melt the entire planetesimal, provided it accreted early. For the reference parameters considered in the manuscript, $\Delta T \sim T_s^{\mathrm{Sil}}$ and a timescale of the order of Myr, the segregation number calculated according to Lichtenberg et al. (2019):

$$R_{seg} = \frac{\tau_{heat}}{\tau_{segr}} = \log_{10} \frac{k_0 \Delta \rho g c_p \Delta T \phi_l}{R \eta_l H_{\mathrm{Al}}(t)}, \tag{A3}$$

is smaller than 1 for a large range of crystal radius, implying inefficient segregation and batch melting (Figure A1b).

Appendix B: Ternary System Forsterite-Anorthite-Diopside

The density of each mineral solid phase was 3,270 kg m^{-3}, 2,760 kg m^{-3}, and 3,200 kg m^{-3} for forsterite, anorthite and diopside, respectively. The density of melt was calculated using partial molar volumes of each individual oxide and their temperature dependence (Niu & Batiza, 1991), while the pressure effect was neglected. The thermal expansion coefficient was 3 10^{-5} K^{-1} and 10^{-4} K^{-1} for the solid minerals and the liquid phase respectively. We show the resulting densities for a typical composition of mass fraction: 60/20/20 forsterite/diopside/anorthite in Figure B2.

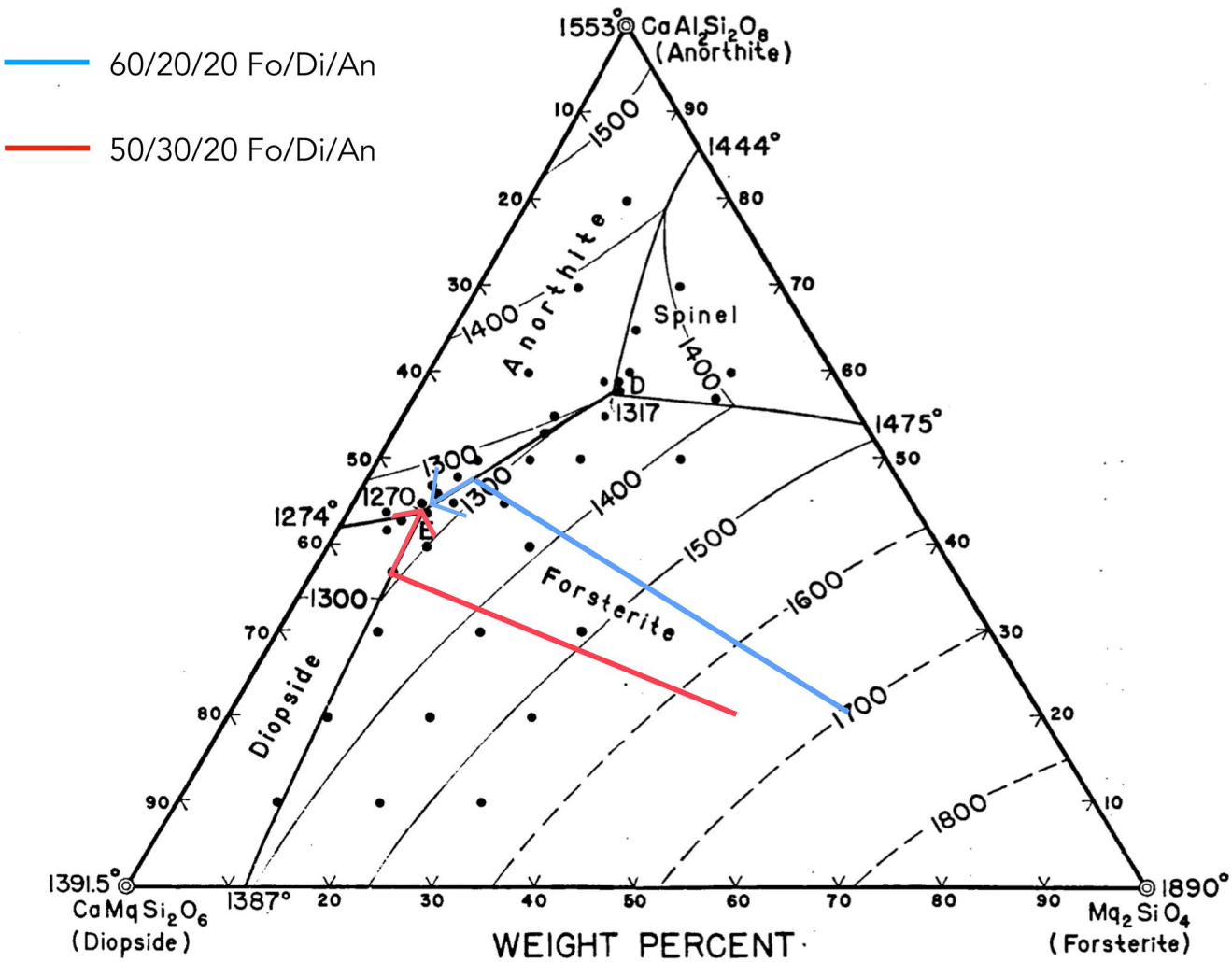

Figure B1. Ternary system used in the model (from Osborn and Tait [1952]).

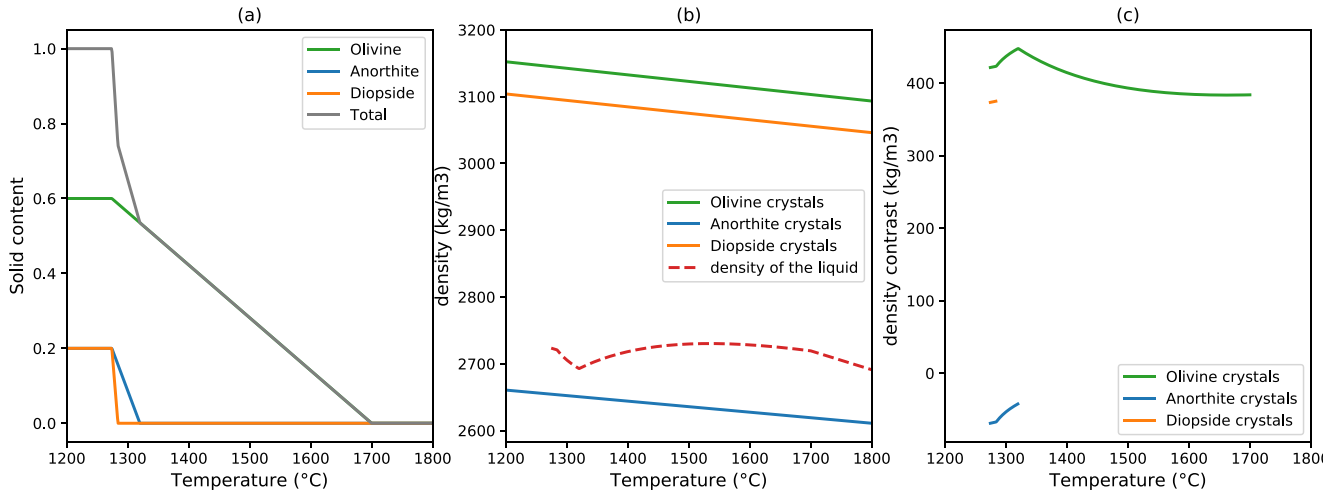

Figure B2. (a) Solid fraction of each mineral in the silicate part of a planetesimal with 60/20/20 Fo/Di/An as a function of temperature, (b) density of each mineral and of the melt during crystallization, and (c) density contrast between the crystals and the melt.

The buoyancy source related to crystal fraction in the cold boundary layer can have greater effect than temperature (Culha et al., 2022). It can be taken into account by considering an effective thermal expansion coefficient (Solomatov, 2015):

$$\alpha' \sim \alpha + \frac{\Delta\rho}{\rho\,(T_l - T_s)} \tag{B1}$$

The effective thermal expansion coefficient α' can be up an order of magnitude larger that the purely thermal one, α, especially for the Diopside crystals characterized by a small difference value between liquidus and solidus temperatures. However, the effect of this parameter on the model output is negligible since the equivalent Rayleigh number is already very high (Ra_H up to 10^{25} for the case illustrated in Figure 3). An order of magnitude change in α would imply an order of magnitude change in Ra_H, but this implies only a few percent change in the maximum heat flux and a negligible difference in the magma ocean episode lifetime (3% and 0.002 Myr respectively, for the model output illustrated in Figure 3).

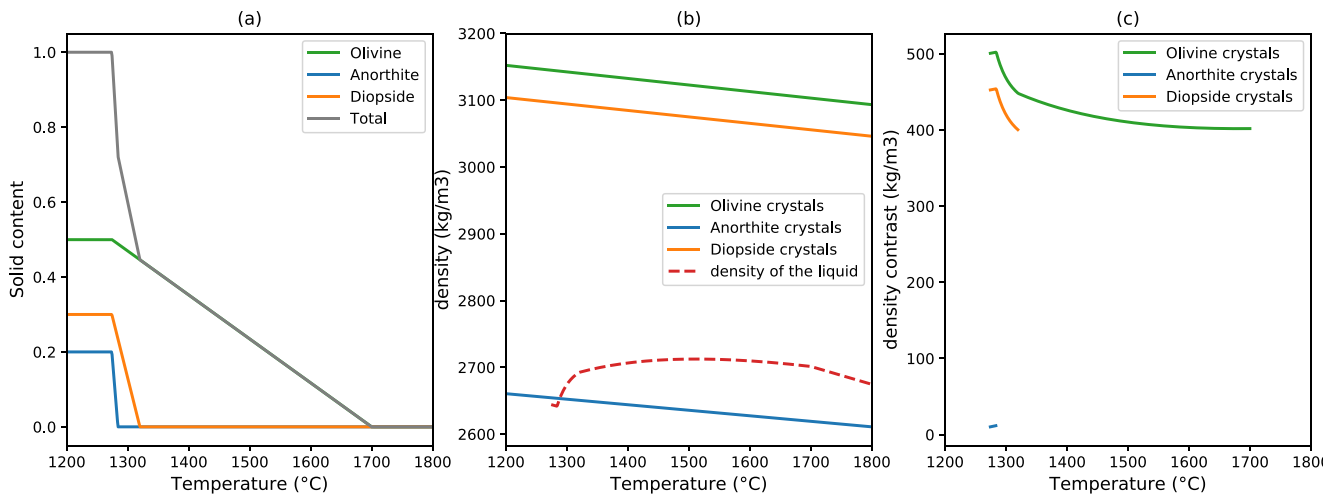

Figure B3. (a) Solid fraction of each mineral in the silicate part of a planetesimal with 50/30/20 Fo/Di/An as a function of temperature, (b) density of each mineral and of the melt during crystallization, (c) density contrast between the crystals and the melt.

For the discussion related to the particular case of Vesta, we also considered the case: 50/30/20 forsterite/diopside/anorthite displayed in Figure B3. In this case, the Anorthite crystals are neutrally buoyant.

Appendix C: Convection Under a Stagnant Lid

The surface and bulk temperatures differ enough for the viscosity to vary by several orders of magnitude. Davaille and Jaupart (1993) proved that in this case the convection occurs under a stagnant lid in which heat is transported by conduction (see Figure C1a). The characteristic temperature scale is given by:

$$\Delta T_v = -C_v \frac{\eta}{\frac{d\eta}{dT}}, \tag{C1}$$

with $C_v = 2.24$.

For the onset of convection, the Rayleigh-Roberts number has to be greater than the critical value of $Ra_{H,c} = 5{,}758$. It has been pointed out that this onset is delayed due to the strong temperature-dependent viscosity (Choblet & Sotin, 2000). The delay time τ_{visc} is given by the relationship:

$$\tau_{visc} = \frac{1}{\pi} \frac{R^2}{\kappa} \left(\frac{Ra_{H,c}}{Ra_H} \right)^{2/3} \left(\frac{T - T_s}{\Delta T_v} \right)^{8/3} \tag{C2}$$

Assuming the rheology (Equations 9 and 10), using also (Equation 30), we get:

$$\Delta T_v(T) = C_v \left[\sigma_{Sil} \frac{\partial \phi}{\partial T} + \frac{E_{a,Sil}}{R_g T^2} \right]^{-1}, \tag{C3}$$

$$\frac{\partial \phi}{\partial T} = \epsilon_{Fo} \frac{\phi_{Fo,0}}{T_l^{Fo} - T_s^{Fo}} + \epsilon_{An} \frac{\phi_{An,0}}{T_l^{An} - T_s^{An}} + \epsilon_{Di} \frac{\phi_{Di,0}}{T_l^{Di} - T_s^{Di}}, \tag{C4}$$

with $\epsilon_i = 1$ if $T_l^i > T > T_s^i$, and 0 otherwise. ΔT_v stands for the drop of temperature in the convective bulk, and is plotted in Figure C1b. Assuming that heat is transported by conduction in the stagnant lid leads to the expression of the stagnant lid thickness:

$$\delta_{SL}(T) = \frac{R}{2} \left(1 - \sqrt{1 - \frac{4k\,(T - \Delta T_v - T_s)}{Q_s R}} \right), \tag{C5}$$

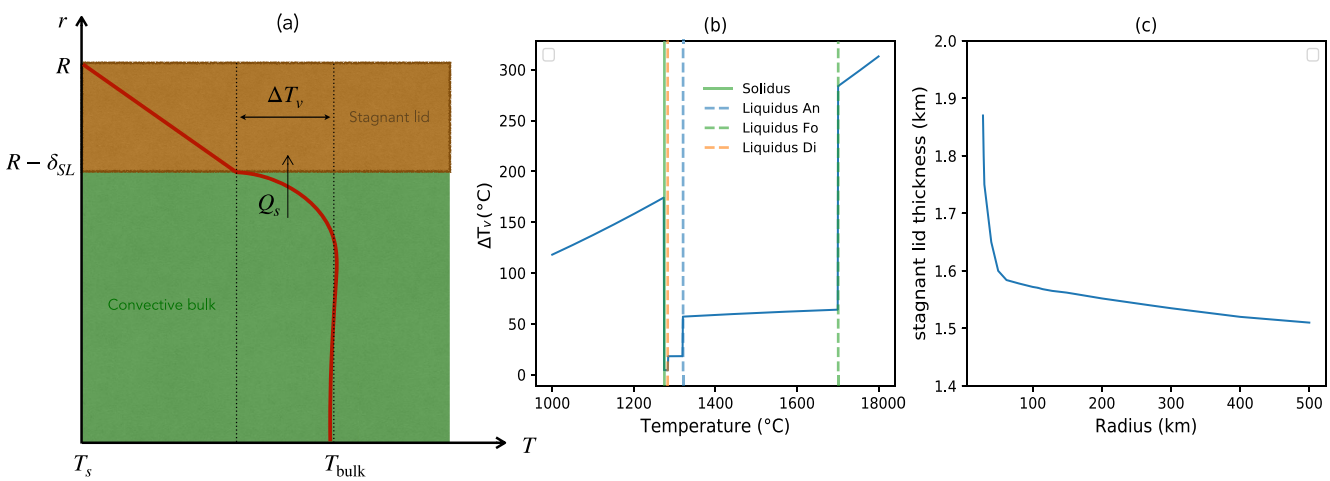

Figure C1. (a) Schematic view of the convective system under a stagnant lid. (b) Temperature drop due to viscous effects as a function of temperature in a magma ocean. (c) Stagnant lid thickness at the rheological transition in a magma ocean as a function of the planetesimals' radius.

with Q_s the basal heat flux entering the stagnant lid. Our model showed that intermediate size planetesimals pass from the conductive state directly to the magma ocean, so the heat flux at the rheological transition is given by the conductive heat flux (Equation 5), which is around $Q_s \sim 1$ W m^{-2} at the end of the conduction stage. In this case the stagnant lid thickness is a function of the temperature and the planetesimal's radius. We can estimate the thickness of the proto-crust at the onset of magma ocean by calculating δ_{SL} ($T = T_{RT}$, R). Results are plotted in Figure C1c, showing that the stagnant lid is ∼1 km thick.

Appendix D: Crystals That Remain in Suspension in the Magma Ocean

We consider a planetesimal of radius R with an iron core of radius R_c. The magma ocean is at temperature T and the volume of light and heavy crystals that crystallize are given respectively by:

$$V_{\rm cr}^{L} = \frac{4}{3}\pi \left(R^3 - R_c^3\right) \phi_{L,\rm cr}, \tag{D1}$$

$$V_{\rm cr}^{H} = \frac{4}{3}\pi \left(R^3 - R_c^3\right) \phi_{H,\rm cr}, \tag{D2}$$

with $\phi_{i,\rm cr}$ given by Equation 30. The magma ocean is sandwiched between a crust of thickness δ_L composed of light crystals (anorthite), and a cumulate of thickness δ_H composed of heavy crystals (forsterite and diopside). The volume occupied by the crust and the cumulate are respectively given by:

$$V_{\rm dep}^{L} = \frac{4}{3}\pi \left[R^3 - (R - \delta_L)^3\right], \tag{D3}$$

$$V_{\rm dep}^{H} = \frac{4}{3}\pi \left[(R_c + \delta_H)^3 - R_c^3\right]. \tag{D4}$$

As the volume of the magma ocean is:

$$V_{\rm MO} = \frac{4}{3}\pi \left[(R - \delta_L)^3 - (R_c + \delta_H)^3\right], \tag{D5}$$

the fraction of light and heavy crystal in suspension are given by $\phi_{i,\rm sus} = \left(V_{\rm cr}^{i} - V_{\rm dep}^{i}\right)/V_{\rm MO}$, so that:

$$\phi_{L,\rm sus} = \frac{\left(1 - f_c^3\right)\phi_{L,\rm cr} - 1 + (1 - \delta_L/R)^3}{(1 - \delta_L/R)^3 - (f_c + \delta_H/R)}, \tag{D6}$$

$$\phi_{H,\rm sus} = \frac{\left(1 - f_c^3\right)\phi_{H,\rm cr} - (f_c + \delta_H/R)^3 + f_c^3}{(1 - \delta_L/R)^3 - (f_c + \delta_H/R)}. \tag{D7}$$

Both the cumulate and the flotation lid are considered to be free of melt.

Conflict of Interest

The authors declare no conflicts of interest relevant to this study.

Data Availability Statement

The script used in this paper is available at Sturtz, Limare, Tait, & Kaminski (2022, https://doi.org/10.5281/zenodo.7181374).

Acknowledgments
This paper is part of Cyril Sturtz's PhD thesis (Université Paris Cité, Institut de Physique du Globe de Paris). The authors would like to thank Norman Sleep, Tobias Keller and two anonymous reviewers for their constructive reviews that improved the manuscript, Laurent Montési for his editorial handling, and Marc Chaussidon for fruitful discussions. This work was supported by the Programme National de Planétologie (PNP) of CNRS/INSU, co-funded by CNES and contributes to the IdEx Université de Paris ANR-18-IDEX-0001.

References

Baker, J., Bizzarro, M., Wittig, N., Connelly, J., & Haack, H. (2005). Early planetesimals melting from an age of 4.5662 Gyr for differentiated meteorites. *Nature*, *436*(7054), 1127–1131. https://doi.org/10.1038/nature03882

Barrat, J.-A., & Ferrière, L. (2021). Olivines in main-group pallasites: Magma-ocean cumulates of partial melting residues? *Geochemical Perspectives Letters*, *16*, 47–52. https://doi.org/10.7185/geochemlet.2103

Bryson, J., Neufeld, J., & Nimmo, F. (2019). Constraints on asteroid magnetic field evolution and the radii of meteorite parent bodies from thermal modelling. *Earth and Planetary Science Letters*, *521*, 68–78. https://doi.org/10.1016/j.epsl.2019.05.046

Carslaw, H. S., & Jaeger, J. C. (1959). *Conduction of heat in solids*. Oxford University Press.

Choblet, G., & Sotin, C. (2000). 3D thermal convection with variable viscosity: Can transient cooling be described by a quasi-static scaling law? *Physics of the Earth and Planetary Interiors*, *119*(3–4), 321–336. https://doi.org/10.1016/s0031-9201(00)00136-9

Clenet, H., Jutsi, M., Barrat, J.-A., Asphaug, E., Benz, W., & Gillet, P. (2014). A deep crust-mantle boundary in the asteroid 4 Vesta. *Nature*, *511*(7509), 303–306. https://doi.org/10.1038/nature13499

Consolmagno, G., Golabek, G., Turrini, D., Jutzi, M., Sirono, S., Svetsov, V., & Tsiganis, K. (2015). Is Vesta an intact and pristine protoplanet? *Icarus*, *254*, 190–201. https://doi.org/10.1016/j.icarus.2015.03.029

Costa, A., Caricchi, L., & Bagdassarov, N. (2009). A model for the rheology of particle-bearing suspensions and partially molten rocks. *Geochemistry, Geophysics, Geosystems*, *10*(3). https://doi.org/10.1029/2008gc002138

Culha, C., Keller, T., & Suckale, J. (2022). Biased witnesses: Crystal thermal records may give conflicting accounts of magma cooling. *Journal of Geophysical Research: Solid Earth*, *127*(5), e2021JB023530. https://doi.org/10.1029/2021jb023530

Davaille, A., & Jaupart, C. (1993). Thermal convection in lava lakes. *Geophysical Research Letters*, *20*(17), 1827–1830. https://doi.org/10.1029/93GL02008

Davies, G. F. (1980). Thermal histories of convective Earth models and constraints on radiogenic heat production in the Earth. *Journal of Geophysical Research*, *85*(B5), 2517–2530. https://doi.org/10.1029/jb085ib05p02517

De Sanctis, M. C., Ammannito, E., Capria, M. T., Tosi, F., Capaccioni, F., Zambon, F., et al. (2012). Spectroscopic characterization of mineralogy and its diversity across Vesta. *Science*, *336*(6082), 697–700. https://doi.org/10.1126/science.1219270

Dodds, K. H., Bryson, J. F. J., Neufeld, J. A., & Harrison, R. J. (2021). The thermal evolution of planetesimals during accretion and differentiation: Consequences for dynamo generation by thermally-driven convection. *Journal of Geophysical Research: Planets*, *126*(3), e2020JE006704. https://doi.org/10.1029/2020JE006704

Elkins-Tanton, L. (2012). Magma oceans in the inner solar system. *Annual Review of Earth and Planetary Sciences*, *40*(1), 113–139. https://doi.org/10.1146/annurev-earth-042711-105503

Elkins-Tanton, L., Burgess, S., & Yin, Q.-Z. (2011). The lunar magma ocean: Reconciling the solidification process with lunar petrology and geochronology. *Earth and Planetary Science Letters*, *304*(3), 326–336. https://doi.org/10.1016/j.epsl.2011.02.004

Elkins-Tanton, L., Weiss, B., & Zuber, M. (2011). Chondrites as samples of differentiated planetesimals. *Earth and Planetary Science Letters*, *305*(1–2), 1–10. https://doi.org/10.1016/j.epsl.2011.03.010

Faroughi, S. A., & Huber, C. (2015). A generalized equation for rheology of emulsions and suspensions of deformable particles subjected to simple shear at low Reynolds number. *Rheologica Acta*, *54*(2), 85–108. https://doi.org/10.1007/s00397-014-0825-8

Giordano, D., Russell, J. K., & Dingwell, D. B. (2008). Viscosity of magmatic liquids: A model. *Earth and Planetary Science Letters*, *271*(1), 123–134. https://doi.org/10.1016/j.epsl.2008.03.038

Golabek, G. J., Bourdon, B., & Gerya, T. V. (2014). Numerical models of the thermomechanical evolution of planetesimals: Application to the acapulcoite-lodranite parent body. *Meteoritics & Planetary Sciences*, *49*(6), 1083–1099. https://doi.org/10.1111/maps.12302

Grasset, O., & Parmentier, E. (1998). Thermal convection in a volumetrically heated, infinite Prandtl number with strongly temperature-dependent viscosity: Implications for planetary thermal evolution. *Journal of Geophysical Research*, *103*(B8), 18171–18181. https://doi.org/10.1029/98jb01492

Guazzelli, E., & Pouliquen, O. (2018). Rheology of dense granular suspensions. *Journal of Fluid Mechanics*, *852*, 852. https://doi.org/10.1017/jfm.2018.548

Haack, H., Rasmussen, K., & Warren, P. H. (1990). Effects of regolith/megaregolith insulation on the cooling history of differentiated asteroids. *Journal of Geophysical Research*, *95*(B4), 5111–5124. https://doi.org/10.1029/jb095ib04p05111

Herzberg, C., Condie, K., & Korenaga, J. (2010). Thermal history of the Earth and its petrological expression. *Earth and Planetary Science Letters*, *292*(1–2), 79–88. https://doi.org/10.1016/j.epsl.2010.01.022

Hevey, P., & Sanders, I. (2006). A model for planetesimal meltdown by 26al and its implications for meteorite parent bodies. *Meteoritics & Planetary Sciences*, *41*(1), 95–106. https://doi.org/10.1111/j.1945-5100.2006.tb00195.x

Höink, T., Schmalzl, J., & Hansen, U. (2006). Dynamics of metal-silicate separation in a terrestrial magma ocean. *Geochemistry, Geophysics, Geosystems*, *7*(9), Q09008. https://doi.org/10.1029/2006GC001268

Howard, L. (1964). Convection at high Rayleigh number. In *Proceedings of the 11th International Congress of Applied Mechanics* (pp. 1109–1115).

Jaumann, R., Williams, D. A., Buczkowski, D. L., Yingst, R. A., Preusker, F., Hiesinger, H., et al. (2012). Vesta's shape and morphology. *Science*, *336*(6082), 687–690. https://doi.org/10.1126/science.1219122

Jutzi, M., Asphaug, E., Gillet, P., Barrat, J. A., & Benz, W. (2013). The structure of the asteroid 4 Vesta as revealed by models of planet-scale collisions. *Nature*, *494*(7436), 207–210. https://doi.org/10.1038/nature11892

Kaminski, E., Limare, A., Kenda, B., & Chaussidon, M. (2020). Early accretion of planetesimals unraveled by the thermal evolution of parent bodies of magmatic iron meteorites. *Earth and Planetary Science Letters*, *548*, 116469. https://doi.org/10.1016/j.epsl.2020.116469

Keller, T., & Suckale, J. (2019). A continuum model of multi-phase reactive transport in igneous systems. *Geophysical Journal International*, *219*(1), 185–222. https://doi.org/10.1093/gji/ggz287

Kruijer, T., Touboul, M., Fischer-Gödde, M., Bermingham, K., Walker, R., & Kleine, T. (2014). Protracted core formation and rapid accretion of protoplanets. *Science*, *344*(6188), 1150–1154. https://doi.org/10.1126/science.1251766

Lavorel, G., & Le Bars, M. (2009). Sedimentation of particles in a vigorously convecting fluid. *Physical Review E: Statistical, Nonlinear, and Soft Matter Physics*, *80*(4), 046324. https://doi.org/10.1103/PhysRevE.80.046324

Lichtenberg, T., Golabek, G. J., Gerya, T. V., & Meyer, M. R. (2016). The effects of short-lived radionuclides and porosity on the early thermo-mechanical evolution of planetesimals. *Icarus*, *274*, 350–365. https://doi.org/10.1016/j.icarus.2016.03.004

Lichtenberg, T., Keller, T., Katz, R. F., Golabek, G. J., & Gerya, T. V. (2019). Magma ascent in planetesimals: Control by grain size. *Earth and Planetary Science Letters*, *507*, 154–165. https://doi.org/10.1016/j.epsl.2018.11.034

Limare, A., Jaupart, C., Kaminski, E., Fourel, L., & Farnetani, C. (2019). Convection in an internally heated stratified heterogeneous reservoir. *Journal of Fluid Mechanics*, *870*, 67–105. https://doi.org/10.1017/jfm.2019.243

Limare, A., Kenda, B., Kaminski, E., Surducan, E., Surducan, V., & Neamtu, C. (2021). Transient convection experiments in internally-heated systems. *MethodsX*, *8*, 101224. https://doi.org/10.1016/j.mex.2021.101224
Mandler, B., & Elkins-Tanton, L. (2013). The origin of eucrites, diogenites, and olivine diogenites: Magma ocean crystallization and shallow magma chamber processes on Vesta. *Meteoritics & Planetary Sciences*, *48*(11), 2333–2349. https://doi.org/10.1111/maps.12135
Marchi, S., McSween, H. Y., O'Brien, D. P., Schenk, P., De Sanctis, M. C., Gaskell, R., et al. (2012). The violent collisional history of asteroid 4 Vesta. *Science*, *336*(6082), 690–694. https://doi.org/10.1126/science.1218757
Martin, D., & Nokes, R. (1989). A fluid-dynamical study of crystal settling in convecting magmas. *Journal of Petrology*, *30*(6), 1471–1500. https://doi.org/10.1093/petrology/30.6.1471
McKenzie, D. (1984). The generation and compaction of partially molten rock. *Journal of Petrology*, *25*(3), 713–765. https://doi.org/10.1093/petrology/25.3.713
McSween, H., Binzel, R., De Sanctis, M., Ammannito, E., Prettyman, T., Beck, A., et al. (2013). Dawn; the Vesta-hed connection; and the geologic context for eucrites, diogenites and howardites. *Meteoritics & Planetary Sciences*, *48*(11), 2090–2104. https://doi.org/10.1111/maps.12108
McSween, H., Raymond, C., Stolper, E., Mittlefehldt, D., Baker, M., Lunning, N., et al. (2019). Differentiation and magmatic history of Vesta: Constraints from HED meteorites and dawn spacecraft data. *Geochemistry*, *79*(4), 125526. https://doi.org/10.1016/j.chemer.2019.07.008
Morbidelli, A., & Raymond, S. N. (2016). Challenges in planet formation. *Journal of Geophysical Research: Planets*, *121*(10), 1962–1980. https://doi.org/10.1002/2016JE005088
Neumann, W., Breuer, D., & Spohn, T. (2012). Differentiation and core formation in accreting planetesimals. *Astronomy & Astrophysics*, *543*, A141. https://doi.org/10.1051/0004-6361/201219157
Neumann, W., Breuer, D., & Spohn, T. (2014). Differentiation of Vesta: Implications for a shallow magma ocean. *Earth and Planetary Science Letters*, *395*, 267–280. https://doi.org/10.1016/j.epsl.2014.03.033
Niu, Y., & Batiza, R. (1991). Denscal: Program for calculating densities of silicate melts and mantle minerals as a function of pressure, temperature, and composition in melting range. *Computers & Geosciences*, *17*(5), 679–687. https://doi.org/10.1016/0098-3004(91)90039-g
Osborn, E., & Tait, D. (1952). The system diopside-forsterite-anorthite. *American Journal of Science*, *250*, 413–433.
Righter, K., & Drake, M. (1997). A magma ocean on Vesta: Core formation and petrogenesis of eucrites and diogenites. *Meteoritics & Planetary Sciences*, *32*(6), 929–944. https://doi.org/10.1111/j.1945-5100.1997.tb01582.x
Roberts, P. (1967). Convection in horizontal layers with internal heat generation. Theory. *Journal of Fluid Mechanics*, *30*(1), 33–49. https://doi.org/10.1017/S0022112067001284
Roeder, P., & Emslie, R. (1970). Olivine-liquid equilibrium. *Contributions to Mineralogy and Petrology*, *29*(4), 275–289. https://doi.org/10.1007/bf00371276
Rubie, D., Melosh, H., Reid, J., Liebske, C., & Righter, K. (2003). Mechanisms of metal-silicate equilibration in the terrestrial magma ocean. *Earth and Planetary Science Letters*, *205*(3), 239–255. https://doi.org/10.1016/s0012-821x(02)01044-0
Russell, C. T., Raymond, C. A., Jaumann, R., McSween, H. Y., De Sanctis, M. C., Nathues, A., et al. (2013). Dawn completes its mission at 4 Vesta. *Meteoritics & Planetary Sciences*, *48*(11), 2076–2089. https://doi.org/10.1111/maps.12091
Sahijpal, S., Soni, P., & Gupta, G. (2007). Numerical simulations of the differentiation of accreting planetesimals with ^{26}Al and ^{60}Fe as the heat sources. *Meteoritics & Planetary Sciences*, *42*(9), 1529–1548. https://doi.org/10.1111/j.1945-5100.2007.tb00589.x
Schubert, G., Turcotte, D., & Olson, P. (2001). *Mantle convection in the Earth and planets*. Cambridge University Press.
Scott, T., & Kohlstedt, D. L. (2006). The effect of large melt fraction on the deformation behavior of peridotite. *Earth and Planetary Science Letters*, *216*(3–4), 177–187. https://doi.org/10.1016/j.epsl.2006.04.027
Simon, J. I., Cuzzi, J. N., McCain, K. A., Cato, M. J., Christoffersen, P. A., Fisher, K. R., et al. (2018). Particle size distributions in chondritic meteorites: Evidence for pre-planetesimal histories. *Earth and Planetary Science Letters*, *494*, 69–82. https://doi.org/10.1016/j.epsl.2018.04.021
Sleep, N. H. (2000). Evolution of the mode of convection within terrestrial planets. *Journal of Geophysical Research*, *105*(E7), 17563–17578. https://doi.org/10.1029/2000je001240
Solomatov, V. S. (2000). Fluid dynamics of a terrestrial magma ocean. *Origin of the Earth and Moon*, *1*, 323–338. https://doi.org/10.2307/j.ctv1v7zdrp.23
Solomatov, V. S. (2015). 9.04 - Magma oceans and primordial mantle differentiation. In G. Schubert (Ed.), *Treatise on geophysics* (2nd ed., pp. 81–104). Elsevier.
Šrámek, O., Milelli, L., Ricard, Y., & Labrosse, S. (2012). Thermal evolution and differentiation of planetesimals and planetary embryos. *Icarus*, *217*(1), 339–354. https://doi.org/10.1016/j.icarus.2011.11.021
Sturtz, C., Kaminski, E., Limare, A., & Tait, S. (2021). The fate of particles in a volumetrically heated convective fluid at high Prandtl number. *Journal of Fluid Mechanics*, *929*, A28. https://doi.org/10.1017/jfm.2021.862
Sturtz, C., Limare, A., Kaminski, E., & Tait, S. (2022). Birth and decline of magma oceans. Part 1: Erosion and deposition of crystal layers in evolving magmatic reservoirs. in revision.
Sturtz, C., Limare, L., Tait, S., & Kaminski, E. (2022). Script used in "birth and decline of magma oceans in planetesimals. Part 2: Structure and thermal history of early accreted small planetary bodies" [Dataset]. Submitted to JGR: Planets. Zenodo. https://doi.org/10.5281/zenodo.7181374
Tang, H., & Dauphas, N. (2012). Abundance, distribution, and origin of ^{60}Fe in the solar plrotoplanetary disk. *Earth and Planetary Science Letters*, *359–360*, 248–263. https://doi.org/10.1016/j.epsl.2012.10.011
Taylor, G. J., & Norman, M. D. (1992). Evidence for magma oceans on asteroids, the Moon, and Earth. In *Physics and chemistry of magma oceans from 1 bar to 4 Mbar* (p. 58).
Townsend, A. A. (1964). Natural convection in water over an ice surface. *Quarterly Journal of the Royal Meteorological Society*, *90*(385), 248–259. https://doi.org/10.1002/qj.49709038503
Warren, P. (1985). The magma ocean concept and lunar evolution. *Annual Review of Earth and Planetary Sciences*, *13*(1), 201–240. https://doi.org/10.1146/annurev.ea.13.050185.001221
Wilson, L., & Goodrich, C. (2012). Melt formation, migration and rapid extraction from differentiated asteroid interiors: Lessons from ureilites extended to all asteroids. In *Lunar and planetary science conference* (p. 1128).
Wilson, L., & Keil, K. (2017). Arguments for the non-existence of magma oceans in asteroids. *Planetesimals: Early differentiation and consequences for planets* (pp. 159–179).
Wood, J. (1970). Petrology of the lunar soil and geophysical implications. *Journal of Geophysical Research*, *75*(32), 6497–6513. https://doi.org/10.1029/JB075i032p06497
Wood, J., Dickey, J., Marvin, U., & Powell, B. (1970). Lunar anorthosites and a geophysical model of the Moon. In *Proceedings of the Apollo 11 Lunar Science Conference* (Vol. *1*, pp. 965–988).

Yamaguchi, A., Barrat, J.-A., Greenwood, R., Shirai, N., Okamoto, C., Setoyanagi, T., et al. (2009). Crustal partial melting on Vesta: Evidence from highly metamorphosed eucrites. *Geochemica et Cosmochimica Acta*, *73*(23), 7162–7182. https://doi.org/10.1016/j.gca.2009.07.037

Yamaguchi, A., Barrat, M., Ito, J.-A., & Bohn, M. (2011). Posteucritic magmatism on Vesta: Evidence from petrology and thermal history of diogenites. *Journal of Geophysical Research*, *116*(E8), E08009. https://doi.org/10.1029/2010je003753

Zuber, M. T., McSween, H. Y., Binzel, R., Elkins-Tanton, L., Konopliv, A., Pieters, C. M., & Smith, D. (2011). Origin, internal structure and evolution of 4 Vesta. *Space Science Reviews*, *163*(1–4), 77–93. https://doi.org/10.1007/s11214-011-9806-8